

A fast spectral method for the Uehling-Uhlenbeck equation for quantum gas mixtures: homogeneous relaxation and transport coefficients

Lei Wu^{a,*}

^a*James Weir Fluids Laboratory, Department of Mechanical and Aerospace Engineering, University of Strathclyde, Glasgow G1 1XJ, UK*

Abstract

A fast spectral method (FSM) is developed to solve the Uehling-Uhlenbeck equation for quantum gas mixtures with generalized differential cross-sections. The computational cost of the proposed FSM is $O(M^{d_v-1}N^{d_v+1}\log N)$, where d_v is the dimension of the problem, M^{d_v-1} is the number of discrete solid angles, and N is the number of frequency nodes in each direction. Spatially-homogeneous relaxation problems are used to demonstrate that the FSM conserves mass and momentum/energy to the machine and spectral accuracy, respectively. Based on the variational principle, transport coefficients such as the shear viscosity, thermal conductivity, and diffusion are calculated by the FSM, which agree well with the analytical solutions. Then, the FSM is applied to find the accurate transport coefficients through an iterative scheme for the linearized quantum Boltzmann equation. The shear viscosity and thermal conductivity of three-dimensional quantum Fermi and Bose gases interacting through hard-sphere potential are calculated. For Fermi gas, the relative difference between the accurate and variational transport coefficients increases with fugacity; for Bose gas, the relative difference in thermal conductivity has similar behavior as the gas moves from the classical to degenerate limits, but the relative difference in shear viscosity decreases when the fugacity increases. Finally, the viscosity and diffusion coefficients have been calculated for a two-dimensional equal-mole mixture of Fermi gases. When the molecular masses of the two components are the same, our numerical results agree with the variational solutions. However, when the molecular mass ratio is not one, large discrepancies between the accurate and variational results are observed; our results are reliable because (i) the method does not rely on any assumption on the form of velocity distribution function and (ii) the ratio between shear viscosity and entropy density satisfies the minimum bound predicted by the string theory.

Keywords: quantum Boltzmann (Uehling-Uhlenbeck) equation, fast spectral method, gas mixture, shear viscosity, thermal conductivity, spin diffusion

*Corresponding author.

E-mail address: lei.wu.100@strath.ac.uk (L. Wu).

1. Introduction

The experimental manipulation of ultracold atomic gases has attracted extensive research interest to understand the dynamics of quantum systems [1]. Most researches focus on the condensed phases [2, 3], since these quantum systems are ideal to study the crossover from a Bardeen-Cooper-Schrieffer superfluid to Bose-Einstein condensation, which is ubiquitous in high-temperature superconductivity, neutron stars, nuclear matter, and quark-gluon plasma. In experiments, however, quantum gases are prepared from dilute classical gases at room temperature, where the thermal motion of gas molecules is described by the Boltzmann equation. As the temperature goes down, the thermal de Broglie wavelength could become comparable to the interatomic distance; in this case the quantum effects emerge, and the thermal motion of quantum gases can be described by the Uehling-Uhlenbeck equation [4], which is also known as the quantum Boltzmann equation (QBE). When the temperature decreases further, the condensation begins, and the condensed phase coexists with the normal phase. For example, for Bose gas, at the temperature below the onset of Bose-Einstein condensation, the QBE and Gross-Pitaevskii equation are used to describe the dynamics of Bose gas in the normal and condensed phases, respectively [5, 6]; the exchange of gas molecules between the normal and condensed phases is also described by the Boltzmann-type collision operators.

Mathematically speaking, the QBE, which is defined in the six-dimensional phase space, is much more complicated than the mean-field Gross-Pitaevskii equation in the three-dimensional physical space. Although in the hydrodynamic regime (i.e. when the mean free path of gas molecules and the characteristic oscillation frequency are respectively much smaller than the characteristic flow length and the mean collision frequency of quantum gases) the Navier-Stokes equation can be derived from the QBE via the Chapman-Enskog expansion [7] to describe the gas dynamics, in quantum experiments, however, this situation is always violated. This is due to the fact that the gas is confined by external potentials, the gas density is very small in the vicinity of the trap so that the gas is highly rarefied. Therefore, to describe the dynamics of quantum gas in the normal phase accurately, an efficient and accurate method to solve the QBE is necessary. In the paper we focus only on the numerical method for QBE.

The direct simulation Monte Carlo method (DSMC) [5, 6, 8] has been proposed to solve the QBE. Since the collision frequency is enhanced (or reduced) for Bose (or Fermi) gas, and this enhancement (or reduction) relies on the velocity distribution function (VDF) after the binary collision, the DSMC method for QBE needs to use a very large number of simulated particles to sample VDF. This is in sharp contrast to the DSMC for classical gases where no such sampling is needed [9]. Moreover, for Fermi gas, due to Pauli's exclusion principle, the collision frequency might become negative (unphysical) if the VDF is not accurately sampled [10]. To reduce the number of simulated particles, Yano proposed to replace the post-collision VDF by the equilibrium VDF [11]. However, in this way, the DSMC solves the Uehling-Uhlenbeck model equation rather than the original QBE, which may introduce large errors when the system is far away from equilibrium as typically occurs in modern experiments of quantum gases [12, 13, 14]. For example, the shear viscosity obtained from the

Uehling-Uhlenbeck model equation is even smaller than the one obtained from the variational solution that predicts the lower bounds of transport coefficients [11].

In recent years, the fast spectral method (FSM), which employs a Fourier-Galerkin discretization in the velocity space and handles binary collisions in the corresponding frequency space, has attracted much attention thanks to its spectral accuracy in solving the Boltzmann collision operator for classical gases [15, 16]. Due to its deterministic nature, it has been successfully applied to accurately calculate the transport coefficients for gas interacting through the Lennard-Jones potentials [17], Couette/Poiseuille/thermal transpiration flows [18, 19, 20], linear oscillatory flows in the rectangular cavity [21, 22], and the spectrum of Rayleigh-Brillouin scattering of the laser-gas interaction [23]. It has also been extended to solve the Boltzmann equation for classical gas mixtures [24, 25], the Enskog equation for dense gases [26, 27], and the QBE for single-species quantum gases [28, 29].

In many recent experiments, quantum gas mixtures, which constitute either of different species or different quantum states of the same species, are used [30, 31, 12, 32]. However, very few numerical methods are developed for quantum gas mixtures. In this paper we propose an efficient and accurate FSM to solve the QBE for quantum gas mixtures.

The rest of this paper is organized as follows. In Sec. 2, the QBE and the equilibrium properties of quantum systems are introduced. In Sec. 3, the FSM is proposed to solve the Boltzmann collision operator with general forms of differential cross-section. Spatially-homogeneous relaxation problems are investigated and factors affecting the accuracy of FSM are identified in Sec. 4. In Sec. 5, the accuracy of FSM is further validated by comparing the transport coefficients obtained from the FSM with variational solutions. Accurate transport coefficients of Fermi gas mixtures are obtained by solving the linearized QBE from the Chapman-Enskog expansion, without using any assumption on the form of VDF. In Sec. 6, we conclude with a summary of the proposed numerical method, and outline future perspectives.

2. The quantum Boltzmann equation of gas mixtures

Consider a system of quantum gas mixtures in the normal phase, so that it can be described semi-classically by the one-particle VDF $f^i(t, \mathbf{x}, \mathbf{v})$, where i denotes the i -th component, t is the time, \mathbf{x} is the spatial coordinate, and \mathbf{v} is the molecular velocity. Since the VDF is defined in the way that $(m^i/2\pi\hbar)^{d_v} f^i(t, \mathbf{x}, \mathbf{v}) d\mathbf{x}d\mathbf{v}$ is the molecular number of i -th component at time t in the phase-space $d\mathbf{x}d\mathbf{p}/(2\pi\hbar)^{d_v} = (m^i/2\pi\hbar)^{d_v} d\mathbf{x}d\mathbf{v}$, macroscopic quantities such as the number density n , bulk velocity \mathbf{V} , shear stress P_{ij} , and heat flux \mathbf{Q} of each component can be calculated as the moments of the corresponding VDF:

$$\begin{aligned} n^i(\mathbf{x}, t) &= \left(\frac{m^i}{2\pi\hbar}\right)^{d_v} \int f^i d\mathbf{v}, & \mathbf{V}^i(\mathbf{x}, t) &= \left(\frac{m^i}{2\pi\hbar}\right)^{d_v} \frac{1}{n^i} \int \mathbf{v} f^i d\mathbf{v}, \\ P_{ij}^i(\mathbf{x}, t) &= \left(\frac{m^i}{2\pi\hbar}\right)^{d_v} m^i \int v_{r,i} v_{r,j} f^i d\mathbf{v}, & \mathbf{Q}^i(\mathbf{x}, t) &= \left(\frac{m^i}{2\pi\hbar}\right)^{d_v} \frac{m^i}{2} \int \mathbf{v}_r |\mathbf{v}_r|^2 f^i d\mathbf{v}, \end{aligned} \quad (1)$$

where m^i is the mass of the i -th component, \hbar is the reduced Planck's constant, $d_v = 2$ or 3 is the dimension of the problem, $\mathbf{v}_r = \mathbf{v} - \mathbf{V}$ is the peculiar velocity, and indexes i and j

79 are Cartesian components of the spatial variable \mathbf{x} . Note that $\mathbf{p} = m^i \mathbf{v}$ is the momentum
80 of gas molecules; we use the velocity \mathbf{v} instead of the momentum \mathbf{p} because it will be easier
81 to develop the FSM that is compatible to our previous works [18, 19, 24, 17, 25, 20].

82 2.1. The quantum Boltzmann equation

83 The QBE is derived from a heuristic argument of the classical Boltzmann equation [4],
84 where the streaming part remains unchanged when compared to that of the classical gas,
85 while the collision operator is modified by quantum laws. For fermions, the collision prob-
86 ability is reduced if the final state that the collision leads to has already been occupied,
87 due to Pauli's exclusion principle. For bosons, on the contrary, the collision probability is
88 enhanced. The QBE takes the form of [4]

$$\frac{\partial f^i}{\partial t} + \mathbf{v} \cdot \frac{\partial f^i}{\partial \mathbf{x}} - \frac{1}{m^i} \frac{\partial U^i}{\partial \mathbf{x}} \cdot \frac{\partial f^i}{\partial \mathbf{v}} = \sum_j \mathcal{Q}^{ij}(f^i, f^j), \quad (2)$$

89 where $U^i(\mathbf{x}, t)$ are the effective potentials acting on the molecules of i -th component, $\mathcal{Q}^{ii}(f^i, f^i)$
90 is the self-collision operator of the i -th component, and $\mathcal{Q}^{ij}(f^i, f^j)$ with $i \neq j$ is the cross-
91 collision operator between the molecules of i -th and j -th components. All the collision
92 operators are local in time and space. For simplicity, t and \mathbf{x} are omitted in writing the
93 collision operators in the following general form:

$$\begin{aligned} \mathcal{Q}^{ij}(f^i, f^j) = & \left(\frac{m^j}{2\pi\hbar} \right)^{d_v} \int_{\mathbb{R}^{d_v}} \int_{\mathbb{S}^{d_v-1}} |\mathbf{u}| \frac{d\sigma^{ij}}{d\Omega} \left\{ f^j({}'\mathbf{v}_*^{ij}) f^i({}'\mathbf{v}^{ij}) [1 + \theta_0 f^j(\mathbf{v}_*)] [1 + \theta_0 f^i(\mathbf{v})] \right. \\ & \left. - f^j(\mathbf{v}_*) f^i(\mathbf{v}) [1 + \theta_0 f^j({}'\mathbf{v}_*^{ij})] [1 + \theta_0 f^i({}'\mathbf{v}^{ij})] \right\} d\Omega d\mathbf{v}_*, \end{aligned} \quad (3)$$

94 where \mathbf{v} and \mathbf{v}_* are the pre-collision velocities of molecules of sorts i and j , respectively,
95 while $'\mathbf{v}^{ij}$, $'\mathbf{v}_*^{ij}$ are the corresponding post-collision velocities. Conservation of momentum
96 and energy yield the following relations

$$'\mathbf{v}^{ij} = \mathbf{v} + \frac{m^j}{m^i + m^j} (|\mathbf{u}| \Omega - \mathbf{u}), \quad '\mathbf{v}_*^{ij} = \mathbf{v}_* - \frac{m^i}{m^i + m^j} (|\mathbf{u}| \Omega - \mathbf{u}), \quad (4)$$

97 where $\mathbf{u} = \mathbf{v} - \mathbf{v}_*$ is the relative pre-collision velocity, Ω is the unit vector in the sphere (or a
98 circle when $d_v = 2$) \mathbb{S}^{d_v-1} having the same direction as the relative post-collision velocity, and
99 θ is the deflection angle between the two relative velocities, i.e. $\cos \theta = \Omega \cdot \mathbf{u} / |\mathbf{u}|$, $0 \leq \theta \leq \pi$.
100 The differential cross-section is given by $d\sigma^{ij}/d\Omega$, which is a function of the relative pre-
101 collision velocity and deflection angle. Finally, the Boltzmann equation for molecules obeying
102 the classical statistics is recovered when $\theta_0 = 0$, while $\theta_0 = 1$ and $\theta_0 = -1$ should be chosen
103 for molecules obeying the quantum Bose-Einstein and Fermi-Dirac statistics, respectively.

104 In the following numerical simulations by FSM, it is convenient to separate the quantum
105 collision operator (3) into the following quadratic and cubic collision operators [28, 29]:

$$\mathcal{Q}^{ij}(f^i, f^j) = \mathcal{Q}_c^{ij} + \theta_0 (\mathcal{Q}_1^{ij} + \mathcal{Q}_2^{ij} - \mathcal{Q}_3^{ij} - \mathcal{Q}_4^{ij}), \quad (5)$$

106 where the classical quadratic collision operator is

$$\mathcal{Q}_c^{ij}(f^i, f^j) = \left(\frac{m^j}{2\pi\hbar}\right)^{d_v} \int_{\mathbb{R}^{d_v}} \int_{\mathbb{S}^{d_v-1}} |\mathbf{u}| \frac{d\sigma^{ij}}{d\Omega} [f^j(\mathbf{v}_*') f^i(\mathbf{v}_*') - f^j(\mathbf{v}_*) f^i(\mathbf{v})] d\Omega d\mathbf{v}_*, \quad (6)$$

107 and the cubic collision operators are

$$\begin{aligned} \mathcal{Q}_1^{ij} &= \left(\frac{m^j}{2\pi\hbar}\right)^{d_v} \int_{\mathbb{R}^{d_v}} \int_{\mathbb{S}^{d_v-1}} |\mathbf{u}| \frac{d\sigma^{ij}}{d\Omega} f^j(\mathbf{v}_*') f^i(\mathbf{v}_*') f^j(\mathbf{v}_*) d\Omega d\mathbf{v}_*, \\ \mathcal{Q}_2^{ij} &= \left(\frac{m^j}{2\pi\hbar}\right)^{d_v} \int_{\mathbb{R}^{d_v}} \int_{\mathbb{S}^{d_v-1}} |\mathbf{u}| \frac{d\sigma^{ij}}{d\Omega} f^j(\mathbf{v}_*') f^i(\mathbf{v}_*') f^i(\mathbf{v}) d\Omega d\mathbf{v}_*, \\ \mathcal{Q}_3^{ij} &= \left(\frac{m^j}{2\pi\hbar}\right)^{d_v} \int_{\mathbb{R}^{d_v}} \int_{\mathbb{S}^{d_v-1}} |\mathbf{u}| \frac{d\sigma^{ij}}{d\Omega} f^j(\mathbf{v}_*') f^j(\mathbf{v}_*) f^i(\mathbf{v}) d\Omega d\mathbf{v}_*, \\ \mathcal{Q}_4^{ij} &= \left(\frac{m^j}{2\pi\hbar}\right)^{d_v} \int_{\mathbb{R}^{d_v}} \int_{\mathbb{S}^{d_v-1}} |\mathbf{u}| \frac{d\sigma^{ij}}{d\Omega} f^i(\mathbf{v}_*') f^j(\mathbf{v}_*) f^i(\mathbf{v}) d\Omega d\mathbf{v}_*. \end{aligned} \quad (7)$$

108 2.2. Equilibrium properties

109 Introducing the entropy density function $s = -\sum_i \left(\frac{m^i}{2\pi\hbar}\right)^{d_v} \int [f^i \ln f^i - \theta_0(1 + \theta_0 f^i) \ln(1 +$
 110 $\theta_0 f^i)] d\mathbf{v}$ to Eq. (2), one can obtain the equilibrium VDF

$$f_{eq}^i(t, \mathbf{x}, \mathbf{v}) = \left\{ \frac{1}{Z^i} \exp \left[\frac{m^i(\mathbf{v} - \mathbf{V})^2}{2k_B T} \right] - \theta_0 \right\}^{-1}, \quad (8)$$

111 where $Z^i(\mathbf{x}, t)$ is the local fugacity satisfying

$$Z^i(\mathbf{x}, t) = \exp \left[\frac{\mu^i(\mathbf{x}, t) - U^i(\mathbf{x}, t)}{k_B T} \right], \quad (9)$$

112 with μ^i and k_B being the chemical potential and Boltzmann constant, respectively.

113 When the quantum system is in equilibrium, we have

$$n^i = \left(\frac{m^i k_B T}{2\pi\hbar^2}\right)^{d_v/2} G_{d_v/2}(Z^i), \quad P_{ij}^i = n^i k_B T \frac{G_{d_v/2+1}(Z^i)}{G_{d_v/2}(Z^i)} \delta_{ij}, \quad (10)$$

114 where δ_{ij} is the Kronecker's delta function, and $G_n(Z) = \frac{1}{\Gamma(n)} \int_0^\infty \frac{y^{n-1}}{Z^{-1}e^y - \theta_0} dy$ is the Bose-
 115 Einstein ($\theta_0 = 1$) or Fermi-Dirac ($\theta_0 = -1$) function, with $\Gamma(n)$ being the Gamma function.

116 It should be noted that, when the fugacity $Z \rightarrow 0$, $G_n(Z) \rightarrow Z$, the quantum gas is in the
 117 near classical limit, where the equilibrium VDF is very close to the Maxwellian equilibrium
 118 VDF for classical gases. Moreover, we have $f^i \sim f_{eq}^i \ll 1$, so the behavior of the quantum
 119 gas is similar to the classical one as the quantum correction term $\theta_0 f^i$ is negligible.

120 *2.3. Linearized collision operators*

121 In some cases it is useful to calculate the linearized quantum collision operator, for
 122 example, to calculate the transport coefficients such as the shear viscosity and thermal
 123 conductivity. When the system slightly deviates from the equilibrium state (8), the one-
 124 particle VDF can be expressed as

$$f^i(t, \mathbf{x}, \mathbf{v}) = f_{eq}^i(\mathbf{x}, \mathbf{v}) + h^i(t, \mathbf{x}, \mathbf{v}), \quad (11)$$

125 where h^i is the disturbance satisfying $|h^i/f_{eq}^i| \ll 1$.

126 The quantum Boltzmann collision operator (3) can be linearized into the following form:

$$\mathcal{L}^{ij}(h^i, h^j) = \sum_j [(\mathcal{L}_{c+}^{ij} - \mu_c^{ij} h^i) + \theta_0(\mathcal{L}_1^{ij} + \mathcal{L}_2^{ij} - \mathcal{L}_3^{ij} - \mathcal{L}_4^{ij})], \quad (12)$$

127 where \mathcal{L}_{c+}^{ij} and μ_c^{ij} are respectively the gain part and the equilibrium collision frequency in
 128 the classical Boltzmann equation that are defined as [19, 17, 25]

$$\begin{aligned} \mathcal{L}_{c+}^{ij} &= \left(\frac{m^j}{2\pi\hbar}\right)^{d_v} \int \int |\mathbf{u}| \frac{d\sigma^{ij}}{d\Omega} [f_{eq}^j(\mathbf{v}_*^{ij}) h^i(\mathbf{v}^{ij}) + h^j(\mathbf{v}_*^{ij}) f_{eq}^i(\mathbf{v}^{ij}) - h^j(\mathbf{v}_*) f_{eq}^i(\mathbf{v})] d\Omega d\mathbf{v}_*, \\ \mu_c^{ij} &= \left(\frac{m^j}{2\pi\hbar}\right)^{d_v} \int \int |\mathbf{u}| \frac{d\sigma^{ij}}{d\Omega} f_{eq}^j(\mathbf{v}_*) d\Omega d\mathbf{v}_*, \end{aligned} \quad (13)$$

129 while the linearized cubic collision operator \mathcal{L}_1^{ij} is obtained by replacing the two VDFs in
 130 \mathcal{Q}_1^{ij} in Eq. (7) with h and f_{eq} and only keeping the linear term of h , in the following manner:

$$\begin{aligned} \mathcal{L}_1^{ij} &= \left(\frac{m^j}{2\pi\hbar}\right)^{d_v} \int_{\mathbb{R}^{d_v}} \int_{\mathbb{S}^{d_v-1}} |\mathbf{u}| \frac{d\sigma^{ij}}{d\Omega} \left[h^j(\mathbf{v}_*^{ij}) f_{eq}^i(\mathbf{v}^{ij}) f_{eq}^j(\mathbf{v}_*) + f_{eq}^j(\mathbf{v}_*^{ij}) h^i(\mathbf{v}^{ij}) f_{eq}^j(\mathbf{v}_*) \right. \\ &\quad \left. + f_{eq}^j(\mathbf{v}_*^{ij}) f_{eq}^i(\mathbf{v}^{ij}) h^j(\mathbf{v}_*) \right] d\Omega d\mathbf{v}_*, \end{aligned} \quad (14)$$

131 the rest cubic collision operators \mathcal{L}_2^{ij} , \mathcal{L}_3^{ij} , and \mathcal{L}_4^{ij} can be obtained in the same way.

132 It is obvious that these linearized collision operators can be solved in the same way as
 133 that for the full collision operators.

134 **3. Fast spectral method for the quantum Boltzmann collision operator**

135 The approximation of the self-collision quadratic operator (6) (i.e. \mathcal{Q}_c^{ij} with $i = j$)
 136 by the FSM has been extensively studied [15, 16, 18, 19], even for generalized forms of
 137 the differential cross-section corresponding to general intermolecular potentials such as the
 138 Lennard-Jones potential [17, 33, 20]. The approximation of the cubic collision operators (7)
 139 with $i = j$ by the FSM has been proposed in Ref. [28, 29], while the approximation for the
 140 cross-collision operator for classical gas mixtures (i.e. \mathcal{Q}_c^{ij} with $i \neq j$ and $m^i \neq m^j$) by the
 141 FSM has been recently developed by the author [24, 25, 20]. In this section, on the basis of
 142 all these numerical methods, we will develop a FSM for the quantum Boltzmann collision
 143 operators with general forms of the differential cross-section, for quantum gas mixtures with
 144 different molecular masses. Specifically, we will solve the cubic cross-collision operators (7)
 145 between the molecules of i -th and j -th components only.

146 *3.1. Carleman-like representation of the collision operator*

147 As usual, we rewrite the collision operators in Eq. (7) using the Carleman-like rep-
 148 resentation. With the following basic identity $2^{d_v-1}|\mathbf{u}|^{2-d_v} \int_{\mathbb{R}^{d_v}} \delta(\mathbf{y} \cdot \mathbf{u} + |\mathbf{y}|^2) f(\mathbf{y}) d\mathbf{y} =$
 149 $|\mathbf{u}|^{d_v-2} \int_{\mathbb{S}^{d_v-1}} f\left(\frac{|\mathbf{u}|\Omega - \mathbf{u}}{2}\right) d\Omega$, where δ is the Dirac delta function, the cubic collision oper-
 150 ator \mathcal{Q}_1^{ij} becomes:

$$\mathcal{Q}_1^{ij} = \int_{\mathbb{R}^{d_v}} \int_{\mathbb{R}^{d_v}} B^{ij}(|\mathbf{y}|, |\mathbf{z}|) \delta(\mathbf{y} \cdot \mathbf{z}) f^j(\mathbf{v} + \mathbf{z} + b^{ij}\mathbf{y}) f^i(\mathbf{v} + a^{ij}\mathbf{y}) f^j(\mathbf{v} + \mathbf{y} + \mathbf{z}) d\mathbf{y} d\mathbf{z}, \quad (15)$$

151 with

$$a^{ij} = \frac{2m^j}{m^i + m^j}, \quad b^{ij} = \frac{m^j - m^i}{m^i + m^j}. \quad (16)$$

152 Note that in the derivation of Eq. (15) we have used the transformations $y = (|\mathbf{u}|\Omega - \mathbf{u})/2$
 153 and $\mathbf{z} = \mathbf{v}_* - \mathbf{v} - \mathbf{y} = -\mathbf{u} - \mathbf{y}$. Therefore, $\mathbf{u} = -\mathbf{y} - \mathbf{z}$ and the deflection angle θ satisfies
 154 $\cos \theta = \Omega \cdot \mathbf{u}/|\mathbf{u}| = -(\mathbf{y} - \mathbf{z}) \cdot (\mathbf{y} + \mathbf{z})/|\mathbf{y} + \mathbf{z}|^2$. Additionally, the delta function $\delta(\mathbf{y} \cdot \mathbf{z})$
 155 poses the condition that the vector \mathbf{z} should be perpendicular to the vector \mathbf{y} , thus we have
 156 $\cos \theta = (|\mathbf{z}|^2 - |\mathbf{y}|^2)/(|\mathbf{y}|^2 + |\mathbf{z}|^2)$ and $\theta = 2\arctan(|\mathbf{y}|/|\mathbf{z}|)$. Since the differential cross-section
 157 $d\sigma^{ij}/d\Omega$ is a function of the relative pre-collision velocity $|\mathbf{u}|$ and the deflection angle θ , B^{ij}
 158 can be expressed as a function of $|y|$ and $|z|$ only:

$$B^{ij} = \left(\frac{m^j}{2\pi\hbar}\right)^{d_v} 2^{d_v-1} |\mathbf{u}|^{3-d_v} \frac{d\sigma^{ij}}{d\Omega} \equiv B^{ij}(|\mathbf{y}|, |\mathbf{z}|). \quad (17)$$

159 In numerical calculations, suppose the distribution functions are supported by a sphere
 160 when $d_v = 3$ (or a disk when $d_v = 2$) of radius S , the relative velocity satisfies $|\mathbf{u}| = |\mathbf{y} + \mathbf{z}| \leq$
 161 $2S$, which leads to $|\mathbf{y}|, |\mathbf{z}| \leq R = \sqrt{2}S$. Therefore, the infinite integration region with respect
 162 to \mathbf{y} and \mathbf{z} is reduced to \mathcal{B}_R , i.e. a sphere (or a disk) of radius R centered at the origin.
 163 Consequently, the collision operator in Eq. (15) is truncated into the following form:

$$\mathcal{Q}_1^{ij} = \int_{\mathcal{B}_R} \int_{\mathcal{B}_R} B^{ij}(|\mathbf{y}|, |\mathbf{z}|) \delta(\mathbf{y} \cdot \mathbf{z}) f^j(\mathbf{v} + \mathbf{z} + b^{ij}\mathbf{y}) f^i(\mathbf{v} + a^{ij}\mathbf{y}) f^j(\mathbf{v} + \mathbf{y} + \mathbf{z}) d\mathbf{y} d\mathbf{z}. \quad (18)$$

164 Similarly, the other cubic collision operators in Eq. (7) are transformed and truncated as

$$\begin{aligned} \mathcal{Q}_2^{ij} &= \int_{\mathcal{B}_R} \int_{\mathcal{B}_R} B^{ij}(|\mathbf{y}|, |\mathbf{z}|) \delta(\mathbf{y} \cdot \mathbf{z}) f^j(\mathbf{v} + \mathbf{z} + b^{ij}\mathbf{y}) f^i(\mathbf{v} + a^{ij}\mathbf{y}) f^i(\mathbf{v}) d\mathbf{y} d\mathbf{z}, \\ \mathcal{Q}_3^{ij} &= \int_{\mathcal{B}_R} \int_{\mathcal{B}_R} B^{ij}(|\mathbf{y}|, |\mathbf{z}|) \delta(\mathbf{y} \cdot \mathbf{z}) f^j(\mathbf{v} + \mathbf{z} + b^{ij}\mathbf{y}) f^j(\mathbf{v} + \mathbf{y} + \mathbf{z}) f^i(\mathbf{v}) d\mathbf{y} d\mathbf{z}, \\ \mathcal{Q}_4^{ij} &= \int_{\mathcal{B}_R} \int_{\mathcal{B}_R} B^{ij}(|\mathbf{y}|, |\mathbf{z}|) \delta(\mathbf{y} \cdot \mathbf{z}) f^i(\mathbf{v} + a^{ij}\mathbf{y}) f^j(\mathbf{v} + \mathbf{y} + \mathbf{z}) f^i(\mathbf{v}) d\mathbf{y} d\mathbf{z}. \end{aligned} \quad (19)$$

165 *3.2. Fast spectral method for truncated collision operators*

166 In FSM, VDFs are periodized on the velocity domain $\mathcal{D}_L = [-L, L]^{d_v}$, where the ve-
 167 locity bound L is chosen to be $L = (3 + \sqrt{2})S/2$ to avoid the aliasing error caused by the
 168 periodization of VDFs and collision operators [34]. In the Fourier spectral method, VDFs
 169 are approximated by the truncated Fourier series,

$$f^i(\mathbf{v}) = \sum_j \hat{f}^i(\xi_j) \exp(i\xi_j \cdot \mathbf{v}), \quad \hat{f}^i(\xi_j) = \frac{1}{(2L)^3} \int_{\mathcal{D}_L} f^i(\mathbf{v}) \exp(-i\xi_j \cdot \mathbf{v}) d\mathbf{v}, \quad (20)$$

170 where i is the imaginary unit, and the frequency components are denoted by

$$\xi = (\xi_1, \xi_2, \dots, \xi_{d_v}) = (j_1, j_2, \dots, j_{d_v}) \frac{\pi}{L} = \mathbf{j} \frac{\pi}{L}, \quad (21)$$

171 with $j_k \in [-N_k/2, -N_k/2 + 1, \dots, N_k/2 - 1]$ and N_k being the number of frequency com-
 172 ponents in the k -th frequency direction.

173 Expanding the truncated collision operators in Eqs. (18) and (19) in the truncated Fourier
 174 series, we find that the \mathbf{j} -th modes $\widehat{\mathcal{Q}}_1^{ij}(\xi_j)$, $\widehat{\mathcal{Q}}_2^{ij}(\xi_j)$, $\widehat{\mathcal{Q}}_3^{ij}(\xi_j)$, and $\widehat{\mathcal{Q}}_4^{ij}(\xi_j)$ are related to the
 175 Fourier coefficients \hat{f}^i and \hat{f}^j as

$$\begin{aligned} \widehat{\mathcal{Q}}_1^{ij}(\xi_j) &= \sum_{\substack{1+\mathbf{m}+\mathbf{n}=\mathbf{j} \\ \mathbf{l}, \mathbf{m}, \mathbf{n}}} \hat{f}_1^i \hat{f}_\mathbf{m}^j \hat{f}_\mathbf{n}^j \beta(a\xi_1 + b\xi_\mathbf{m} + \xi_\mathbf{n}, \xi_\mathbf{m} + \xi_\mathbf{n}), \\ \widehat{\mathcal{Q}}_2^{ij}(\xi_j) &= \sum_{\substack{1+\mathbf{m}+\mathbf{n}=\mathbf{j} \\ \mathbf{l}, \mathbf{m}, \mathbf{n}}} \hat{f}_1^i \hat{f}_\mathbf{m}^j \hat{f}_\mathbf{n}^i \beta(a\xi_1 + b\xi_\mathbf{m}, \xi_\mathbf{m}), \\ \widehat{\mathcal{Q}}_3^{ij}(\xi_j) &= \sum_{\substack{1+\mathbf{m}+\mathbf{n}=\mathbf{j} \\ \mathbf{l}, \mathbf{m}, \mathbf{n}}} \hat{f}_1^i \hat{f}_\mathbf{m}^j \hat{f}_\mathbf{n}^i \beta(\xi_\mathbf{m} + a\xi_\mathbf{n}, \xi_\mathbf{m}), \\ \widehat{\mathcal{Q}}_4^{ij}(\xi_j) &= \sum_{\substack{1+\mathbf{m}+\mathbf{n}=\mathbf{j} \\ \mathbf{l}, \mathbf{m}, \mathbf{n}}} \hat{f}_1^i \hat{f}_\mathbf{m}^j \hat{f}_\mathbf{n}^j \beta(\xi_\mathbf{m} + b\xi_\mathbf{n}, \xi_\mathbf{m} + \xi_\mathbf{n}), \end{aligned} \quad (22)$$

176 where the kernel mode $\beta(\mathbf{l}, \mathbf{m})$ is

$$\beta(\xi_1, \xi_\mathbf{m}) = \int_{\mathcal{B}_R} \int_{\mathcal{B}_R} B^{ij}(|\mathbf{x}|, |\mathbf{y}|) \delta(\mathbf{y} \cdot \mathbf{z}) \exp(i\xi_1 \cdot \mathbf{y} + i\xi_\mathbf{m} \cdot \mathbf{z}) dy dz. \quad (23)$$

177 Note that the direct calculation of each term in Eq. (22) is time-consuming, at the order
 178 of N^{3d_v} . Our goal in the following subsection is to separate ξ_1 and $\xi_\mathbf{m}$ in the kernel mode
 179 $\beta(\xi_1, \xi_\mathbf{m})$ so that Eq. (22) can be calculated effectively by the FFT-based convolution, with
 180 a much lower computational cost.

181 *3.2.1. Approximation of the kernel mode*

182 Introducing $\mathbf{y} = \rho \mathbf{e}$ and $\mathbf{z} = \rho' \mathbf{e}'$, where \mathbf{e} and \mathbf{e}' are vectors in the unit sphere when
 183 $d_v = 3$ and unit circle when $d_v = 2$. The kernel mode (23) is expressed in the spherical

184 ($d_v = 3$) or polar ($d_v = 2$) coordinates as

$$\begin{aligned}
& \int \int \delta(\mathbf{e} \cdot \mathbf{e}') \int_0^R \int_0^R (\rho\rho')^{d_v-2} B^{vj}(\rho, \rho') \exp(i\rho\xi_1 \cdot \mathbf{e}) \exp(i\rho'\xi_{\mathbf{m}} \cdot \mathbf{e}') d\rho' d\rho d\mathbf{e}' d\mathbf{e} \\
&= \sum_{r=1}^{M_2} \int \int \delta(\mathbf{e} \cdot \mathbf{e}') \int_0^R \omega_r(\rho_r\rho')^{d_v-2} B^{vj}(\rho_r, \rho') \exp(i\rho_r\xi_1 \cdot \mathbf{e}) \exp(i\rho'\xi_{\mathbf{m}} \cdot \mathbf{e}') d\rho' d\mathbf{e}' d\mathbf{e} \\
&= \sum_{r=1}^{M_2} \int \int \delta(\mathbf{e} \cdot \mathbf{e}') \exp(i\rho_r\xi_1 \cdot \mathbf{e}) \phi(\rho'_r, \xi_{\mathbf{m}} \cdot \mathbf{e}') d\mathbf{e}' d\mathbf{e}, \tag{24}
\end{aligned}$$

185 where the integral with respect to ρ has been approximated by the Gauss-Legendre quadra-
186 ture, with ρ_r and ω_r ($r = 1, 2, \dots, M_2$) being respectively the abscissas and weights of the
187 Gauss-Legendre quadrature in the region of $0 \leq \rho \leq R$, and the term

$$\phi(\rho'_r, \xi_{\mathbf{m}} \cdot \mathbf{e}') = \int_0^R \omega_r(\rho_r\rho')^{d_v-2} B^{vj}(\rho_r, \rho') \cos(\rho'\xi_{\mathbf{m}} \cdot \mathbf{e}') d\rho', \tag{25}$$

188 can be calculated accurately by some high order numerical quadrature.

189 It should be highlighted that the maximum value of $\rho_r\xi_1 \cdot \mathbf{e}$ in Eq. (24) is $N\pi R/2L$.
190 Therefore, the function $\exp(i\rho_r\xi_1 \cdot \mathbf{e})$ oscillates N times at the most. Consequently, M_2
191 should be roughly of the order of N to make the integral with respect to ρ in Eq. (24)
192 by the Gauss-Legendre quadrature accurate. In practical calculation, however, since the
193 spectra of the VDF and the kernel model at high frequency components are very small, M_2
194 can be several times smaller than N to have better numerical efficiency; this point will be
195 demonstrated in the numerical simulation in Sec. 4. Also, note that in the evaluation of the
196 integral with respect to ρ' , the imaginary part is omitted due to the symmetry condition,
197 that is, B^{vj} , which is related to the differential cross-section, remains unchanged when \mathbf{e}' is
198 replaced by $-\mathbf{e}'$, see Eq (17).

199 After some algebraic manipulation (see descriptions from Eq. (34) to Eq. (38) in Ref. [18]
200 when $d_v = 3$, and Eqs. (15) and (16) in Ref. [26] when $d_v = 2$), we have

- 201 • when $d_v = 3$, the integral with respect to the unit vector \mathbf{e} in a sphere is approximated
202 by the trapezoidal rule, i.e. $e_{\theta_p, \varphi_q} = (\sin \theta_p \cos \varphi_q, \sin \theta_p \sin \varphi_q, \cos \theta_p)$ with $\theta_p = p\pi/M$
203 and $\varphi_q = q\pi/M$, where $p, q = 1, 2, \dots, M$, and the kernel mode (24) can be approxi-
204 mated by:

$$\beta(\mathbf{l}, \mathbf{m}) \simeq \frac{2\pi^2}{M^2} \sum_{r,p,q=1}^{M_2, M-1, M} \cos(\rho_r\xi_1 \cdot \mathbf{e}_{\theta_p, \varphi_q}) \psi_3 \left(\rho_r, \sqrt{|\xi_{\mathbf{m}}|^2 - (\xi_1 \cdot \mathbf{e}_{\theta_p, \varphi_q})^2} \right) \sin \theta_p, \tag{26}$$

205 where $\psi_3(\rho_r, s) = 2\pi \int_0^R \omega_r \rho_r \rho' B^{vj}(\rho_r, \rho') J_0(\rho' s) d\rho'$, with J_0 being the zeroth-order
206 Bessel function of first kind.

- 207 • when $d_v = 2$, the integral with respect to the unit vector \mathbf{e} in a circle is approximated by
208 the trapezoidal rule, i.e. $e_{\theta_p} = (\cos \theta_p, \sin \theta_p)$ with $\theta_p = p\pi/M$, where $p = 1, 2, \dots, M$,

209

and the kernel mode (24) is approximated by

$$\beta(\mathbf{l}, \mathbf{m}) \simeq \frac{\pi}{M} \sum_{r,p=1}^{M_2, M} \cos(\rho_r \xi_{\mathbf{l}} \cdot \mathbf{e}_{\theta_p}) \psi_2(\rho_r, \xi_{\mathbf{m}} \cdot \mathbf{e}_{\theta_p + \frac{\pi}{2}}), \quad (27)$$

210

where $\psi_2(\rho_r, s) = 4 \int_0^R \omega_r B^{vj}(\rho_r, \rho') \cos(\rho' \xi_{\mathbf{m}} \cdot \mathbf{e}') d\rho'$.

211

From Eqs. (26) and (27), we see that $\xi_{\mathbf{l}}$ and $\xi_{\mathbf{m}}$ are separated into two different functions, which enables fast computation of the quantum collision operator via the FFT-based convolution. The major algorithm is described below.

214

3.3. Detailed numerical implementation

215

We take the 2D case as an example to demonstrate how the FSM is implemented. First

216

the cosine function in Eq. (27) is expressed in terms of the exponential function:

$$\cos(\rho_r \xi_{\mathbf{l}} \cdot \mathbf{e}_{\theta_p}) = \frac{\exp(i\rho_r \xi_{\mathbf{l}} \cdot \mathbf{e}_{\theta_p}) + \exp(-i\rho_r \xi_{\mathbf{l}} \cdot \mathbf{e}_{\theta_p})}{2}, \quad (28)$$

217

and for simplicity only the term related to $\exp(i\rho_r \xi_{\mathbf{l}} \cdot \mathbf{e}_{\theta_p})$ is considered in this subsection, as the term related to $\exp(-i\rho_r \xi_{\mathbf{l}} \cdot \mathbf{e}_{\theta_p})$ can be handled similarly.

219

The spectrum of the cubic collision operators \mathcal{Q}_1 can be expressed as

$$\begin{aligned} \widehat{\mathcal{Q}}_1^{vj}(\xi_{\mathbf{j}}) &\simeq \frac{\pi}{M} \sum_{r,p=1}^{M_2, M} \sum_l \exp(ia\rho_r \xi_l \cdot \mathbf{e}_{\theta_p}) \hat{f}_1^i \\ &\times \underbrace{\sum_{\substack{\mathbf{m}+\mathbf{n}=\mathbf{j}-1 \\ m,n}} \exp(ib\rho_r \xi_{\mathbf{m}} \cdot \mathbf{e}_{\theta_p}) \hat{f}_{\mathbf{m}}^j \times \exp(i\rho_r \xi_{\mathbf{n}} \cdot \mathbf{e}_{\theta_p}) \hat{f}_{\mathbf{n}}^j \psi_2(\rho_r, \xi_{\mathbf{m}+\mathbf{n}} \cdot \mathbf{e}_{\theta_p + \frac{\pi}{2}})}_{C_2^{rp}(\mathbf{m}+\mathbf{n})}, \end{aligned} \quad (29)$$

220

221

222

223

224

225

226

227

where the underlined term is a convolution that can be computed via FFT with a cost of $O(N^2 \log N)$, and the result of which multiplied by $\psi_2(\rho_r, \xi_{\mathbf{m}+\mathbf{n}} \cdot \mathbf{e}_{\theta_p + \frac{\pi}{2}})$ forms $C_2^{rp}(\mathbf{m}+\mathbf{n})$. The terms $C_2^{rp}(\mathbf{m}+\mathbf{n})$ and $\exp(ia\rho_r \xi_l \cdot \mathbf{e}_{\theta_p}) \hat{f}_1^i$ form the convolution again, which can be calculated by FFT again with a cost of $O(N^2 \log N)$. Since this convolution has to be repeated MM_2 times, the total computational cost will be $O(MN^3 \log N)$, as M_2 should be at the order of N , see the paragraph after Eq. (25).

When C_2^{rp} in Eq. (29) is obtained, the spectrum of the cubic collision operator \mathcal{Q}_4 can be expressed as:

$$\widehat{\mathcal{Q}}_4^{vj}(\xi_{\mathbf{j}}) \simeq \frac{\pi}{M} \sum_l \hat{f}_1^i \times \sum_{r,p=1}^{M_2, M} C_2^{rp}(\mathbf{j}-\mathbf{l}). \quad (30)$$

228

which can be calculated by FFT with the cost $O(N^2 \log N)$.

229

To calculate $\widehat{\mathcal{Q}}_2^{vj}$, we first introduce

$$C_1^{rp}(\mathbf{l}+\mathbf{m}) = \exp(ia\rho_r \xi_{\mathbf{l}} \cdot \mathbf{e}_{\theta_p}) \hat{f}_1^i \times \exp(ib\rho_r \xi_{\mathbf{m}} \cdot \mathbf{e}_{\theta_p}) \psi_2(\rho_r, \xi_{\mathbf{m}} \cdot \mathbf{e}_{\theta_p + \frac{\pi}{2}}) \hat{f}_{\mathbf{m}}^j, \quad (31)$$

230 which is a convolution between the function $\exp(ia\rho_r\xi_{\mathbf{1}}\cdot\mathbf{e}_{\theta_p})\hat{f}_{\mathbf{1}}^i$ and $\exp(ib\rho_r\xi_{\mathbf{m}}\cdot\mathbf{e}_{\theta_p})\psi_2(\rho_r,\xi_{\mathbf{m}}\cdot$
 231 $\mathbf{e}_{\theta_p+\frac{\pi}{2}})\hat{f}_{\mathbf{m}}^j$. Then, the spectrum of the cubic collision operator \mathcal{Q}_2^{ij} can be expressed as

$$\widehat{\mathcal{Q}}_2^{ij}(\xi_{\mathbf{j}}) \simeq \frac{\pi}{M} \sum_{\mathbf{n}} \hat{f}_{\mathbf{n}}^i \times \sum_{r,p=1}^{M_2,M} C_1^{rp}(\mathbf{j}-\mathbf{n}), \quad (32)$$

232 which can be solved by the FFT-based convolution; the total computational cost should be
 233 $O(MM_2N^2 \log N)$, since C_1^{rp} needs to be evaluated MM_2 times, which is at the order of
 234 $MN^3 \log N$.

235 The spectral of the cubic collision operator \mathcal{Q}_3 , as given in Eq. (22), can be expressed as:

$$\widehat{\mathcal{Q}}_3^{ij}(\xi_{\mathbf{j}}) \simeq \frac{\pi}{M} \sum_l \hat{f}_{\mathbf{l}}^i \sum_{r,p=1}^{M_2,M} \sum_{\substack{\mathbf{m}+\mathbf{n}=\mathbf{j}-\mathbf{l} \\ m,n}} \exp(ia\rho_r\xi_{\mathbf{n}}\cdot\mathbf{e}_{\theta_p})\hat{f}_{\mathbf{n}}^i \times \exp(i\rho_r\xi_{\mathbf{m}}\cdot\mathbf{e}_{\theta_p})\hat{f}_{\mathbf{m}}^j \psi_2(\rho_r,\xi_{\mathbf{m}}\cdot\mathbf{e}_{\theta_p+\frac{\pi}{2}}), \quad (33)$$

236 where the computational cost will be $O(MN^3 \log N)$, like $\widehat{\mathcal{Q}}_1^{ij}$.

237 When $\widehat{\mathcal{Q}}^{ij}$ is obtained, the collision operator \mathcal{Q}^{ij} can be obtained through the following
 238 FFT, with a cost $O(N^2 \log N)$:

$$\mathcal{Q}^{ij}(\mathbf{v}) = \sum_{\mathbf{j}} \widehat{\mathcal{Q}}^{ij}(\xi_{\mathbf{j}}) \exp(i\xi_{\mathbf{j}}\cdot\mathbf{v}). \quad (34)$$

239 Therefore, if the FFT-based convolution is applied, for the case of $d_v = 2$, the over-
 240 all computational cost is $O(MN^3 \log N)$, while for $d_v = 3$, the computational cost is
 241 $O(M^2N^4 \log N)$. Note that the procedure in deriving the FSM for QBE is essentially the
 242 same as that for the classical Boltzmann equation, therefore, it can be proved that the present
 243 FSM conserves the mass and satisfies the H-theorem, while errors on the approximations of
 244 momentum and energy are spectrally small [15, 16].

245 4. The spatially-homogeneous relaxation of quantum gases

246 In this section, we assess the performance of FSM in the study of spatially-homogeneous
 247 relaxation of binary gas mixtures of components A and B . Since the property of self-collision
 248 operators has been well investigated [18, 16, 29], we focus on the cross-collision collision
 249 operators only. This situation actually occurs in Fermi gases where interactions between
 250 fermions with the same spin (i.e. described by the self-collision operator) are much smaller
 251 than those between opposite spins (i.e. described by the cross-collision operator) [12, 35, 36].
 252 For simplicity, we consider the case of $d_v = 2$, with the following differential cross-section [35]:

$$\frac{d\sigma^{ij}}{d\Omega} = \frac{2\pi\hbar}{m_r|\mathbf{u}|} \frac{1}{\log^2(a_s^2 m_r^2 |\mathbf{u}|^2 / \hbar^2) + \pi^2}, \quad (35)$$

253 where a_s is the s-wave scattering length that can be controlled experimentally via Feshbach
 254 resonance, and $m_r = m^A m^B / (m^A + m^B)$ is the reduced mass.

255 The evolution of VDFs for components A and B in the spatially-homogeneous relaxation
 256 is governed by the following equations

$$\frac{\partial f^A}{\partial t'} = Q^{AB}(f^A, f^B), \quad \frac{\partial f^B}{\partial t'} = Q^{BA}(f^B, f^A), \quad (36)$$

257 with the following cross-collision operator

$$\begin{aligned} \mathcal{Q}^{ij}(f^i, f^j) = & \left(\frac{m^j}{m^A}\right)^2 \int \int \frac{d\Omega d\mathbf{v}_*}{\log^2(a|\mathbf{u}|^2) + \pi^2} \left\{ f^j(\mathbf{v}_*) f^i(\mathbf{v}^{ij}) [1 + \theta_0 f^j(\mathbf{v}_*)] [1 + \theta_0 f^i(\mathbf{v})] \right. \\ & \left. - f^j(\mathbf{v}_*) f^i(\mathbf{v}) [1 + \theta_0 f^j(\mathbf{v}_*)] [1 + \theta_0 f^i(\mathbf{v}^{ij})] \right\}, \end{aligned} \quad (37)$$

258 where $t' = tm^A k_B T_r / \pi \hbar m_r$, $a = 2k_B T_r a_s^2 m_r^2 / m^A$, and the velocity have been normalized
 259 by $\sqrt{2k_B T_r / m^A}$, with T_r being the reference temperature. We will study how the initial
 260 non-equilibrium VDFs

$$f^A(t=0, \mathbf{v}) = f^B(t=0, \mathbf{v}) = \frac{8}{\pi} |\mathbf{v}|^2 \exp(-|\mathbf{v}|^2), \quad (38)$$

261 relax to the final equilibrium states.

262 4.1. The equal-mass mixture

263 Since the mass and energy are conserved during the collision, for the equal-mass case
 264 (i.e. $m^A = m^B$), the final equilibrium state corresponding to the initial condition (38) is

$$f^A(t=\infty, \mathbf{v}) = f^B(t=\infty, \mathbf{v}) = \left\{ \frac{1}{Z} \exp\left(\frac{|\mathbf{v}|^2}{T}\right) - \theta_0 \right\}^{-1}, \quad (39)$$

265 where the equilibrium fugacity and temperature (Z, T) are $(7.0363, 1.2219)$, $(1.2732, 2.0000)$,
 266 and $(0.6291, 2.5671)$ for the Fermi, classical, and Bose gases, respectively.

267 Figure 1 depicts the relaxation-to-equilibrium process of VDFs, as well as the time evo-
 268 lution of the fourth- and sixth-order moments, when Eq. (36) is solved by the Euler method
 269 with a time-step of 0.0025, and the collision operator (37) is approximated by the FSM with
 270 the following parameters: the number of solid angle is discretized uniformly with $M = 10$,
 271 the velocity domain $[-L, L]^2$ with $L = 6$ is discretized by $N = 64$ uniform grid points
 272 in each direction, and $M_2 = 64$ is chosen in the Gauss-Legendre approximation used in
 273 Eq. (24). It can be seen from Fig. 1(a,b,c) that the final equilibrium states agree well with
 274 the analytical solutions (39). Mathematically, it has been proven that the FSM preserves
 275 the mass accurately for the classical Boltzmann equation, while the energy is conserved with
 276 spectral accuracy [15]; from the numerical simulation with the above detailed parameters,
 277 these conclusions hold also for the QBE. For example, for Fermi gas the maximum rela-
 278 tive variations in mass and energy during the whole relaxation process are 2.7×10^{-15} and
 279 4.4×10^{-7} , respectively. Thus, the VDF, as well as its fourth- and sixth-order moments, are
 280 chosen as reference solutions to investigate factors that affect the accuracy of FSM, such

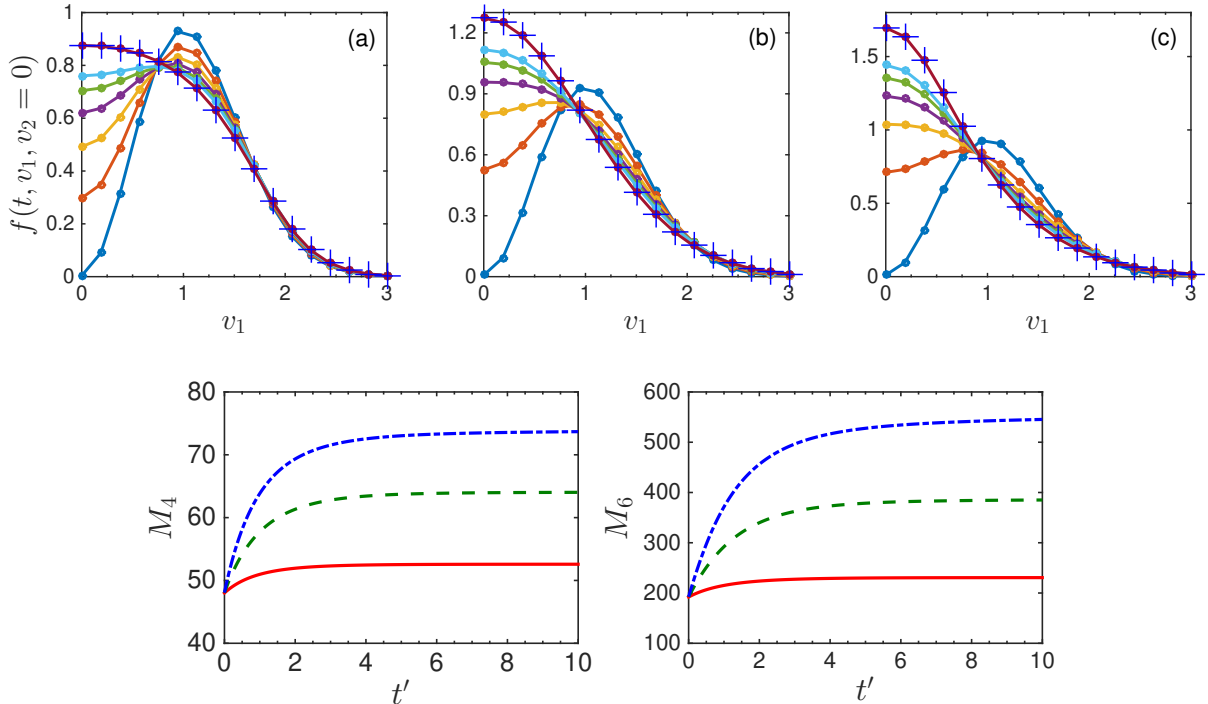


Figure 1: (top row) The spatially-homogeneous relaxation of VDFs for (a) Fermi, (b) classical, and (c) Bose gases, where the differential cross-section is given by Eq. (35) with the normalized parameter $a = 1$ in Eq. (37). Due to symmetry, only the region $v_1 > 0$ is shown. In each subfigure, from bottom to top (near $v_1 = 0$), the time t' for each line is 0, 0.25, 0.50, 0.75, 1, 1.25, and 10, respectively. The symbol ‘cross’ shows the equilibrium VDF (39). (bottom) The time evolution of the fourth- and sixth-order moments of the VDF: $M_4(t) = \int \int f(\mathbf{v}, t) |\mathbf{v}|^4 d\mathbf{v}$ and $M_6(t) = \int \int f(\mathbf{v}, t) |\mathbf{v}|^6 d\mathbf{v}$. Solid, dashed, and dash-dotted lines are the results for Fermi, classical, and Bose gases.

281 as the number of discrete velocities N , discrete solid angles M , and the value of M_2 in the
 282 Gauss-Legendre quadrature.

283 Figure 2 shows the absolute error in the VDF when the velocity grids are kept at $64 \times$
 284 64 , while values of M and M_2 are reduced. When the value of M_2 is fixed, it is seen
 285 that decreasing the number of discrete solid angle M from 10 to 5 affects only slightly
 286 the accuracy. Therefore, $M = 5$ can be considered accurate, as it has been chosen in our
 287 previous numerical simulations of the classical Boltzmann equation [18, 19]. The value of
 288 M_2 , however, strongly affects the accuracy. Theoretically, M_2 should be at the order of N
 289 to make the approximation in Eq. (24) sufficiently accurate for each frequency component,
 290 see the paragraph after Eq. (25). However, at large frequency components the kernel mode
 291 $\beta(\mathbf{l}, \mathbf{m})$ in Eq. (27) and the spectrum of the VDF are sufficiently small, therefore, M_2 can
 292 be smaller than N : in Fig. 2 it is seen that even $M_2 = 10$ has good accuracy.

293 Figure 3 shows the relative errors of the zeroth-, second-, fourth-, and sixth-order mo-
 294 ments of the VDF as functions of the time. Odd-order moments are not included because
 295 they are zero due to the symmetry in VDF. From this figure we can see that the accuracy
 296 deteriorates when the number of velocity points and frequency components N^2 decreases.

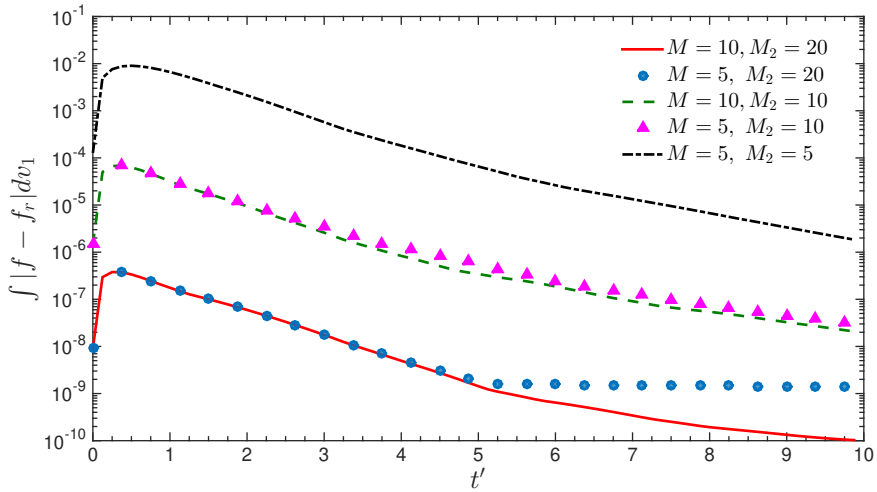


Figure 2: The relative error in the mesoscopic VDF of Fermi gas evaluated at $v_2 = 0$, when the velocity space $[-6, 6]^2$ is discretized by 64×64 uniform points. Note that the reference solution f_r is obtained by the FSM with the same parameters as used in Fig. 1.

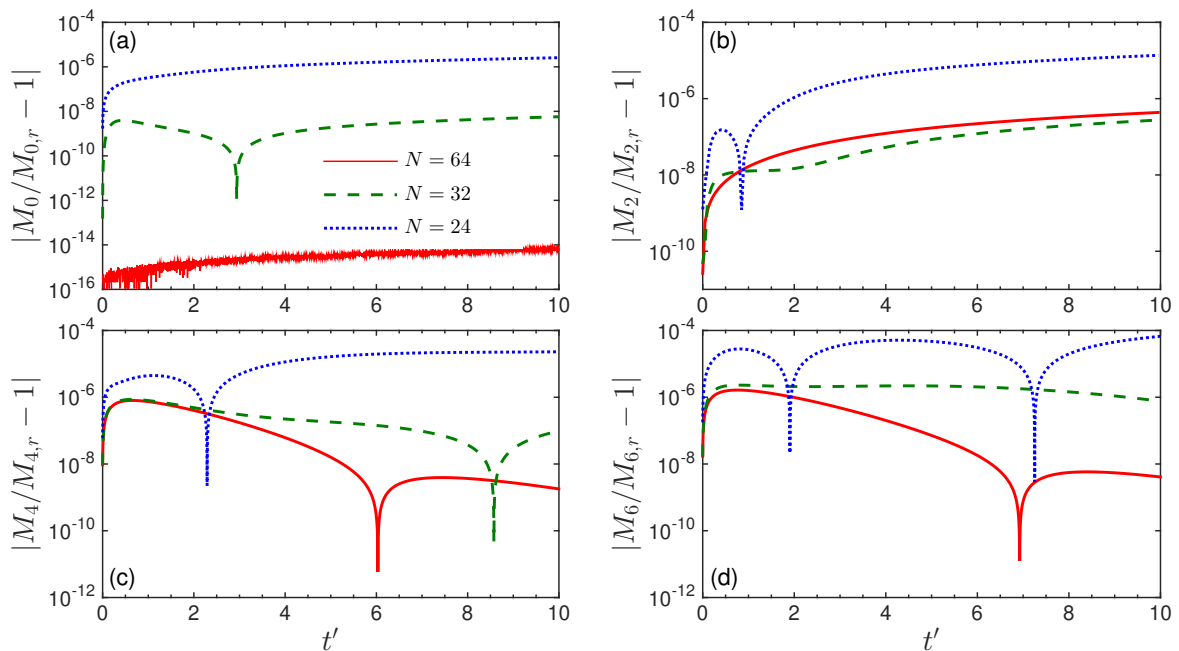


Figure 3: The relative errors of the zeroth-, second-, fourth- and sixth-order moments of the VDF of Fermi gas as compared to the reference solutions with $N = M_2 = 64$. $M = 5$ and $M_2 = 10$ are chosen, while other parameters are the same as in Fig. 1. Note that $M_{0,r}$ and $M_{2,r}$ are calculated based on the initial VDF, since theoretically the mass and energy is conserved during the homogeneous relaxation.

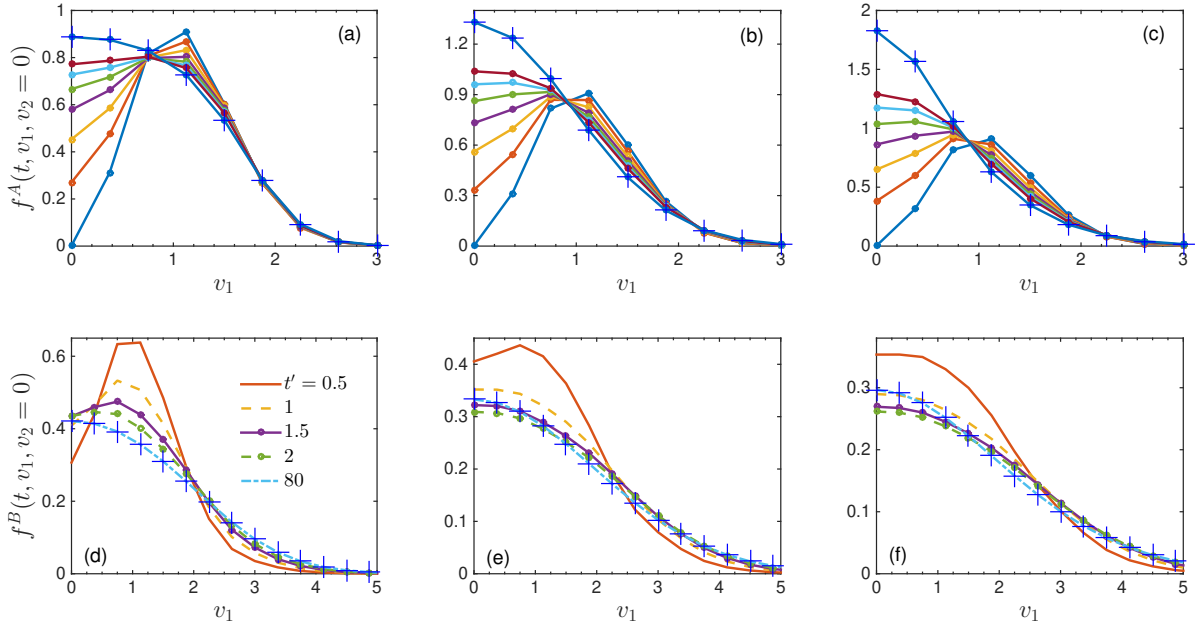


Figure 4: The relaxation of VDFs in the binary mixture with $m^A/m^B = 4$. (top row) The spatially-homogeneous relaxation of VDFs f^A for (a) Fermi, (b) classical, and (c) Bose gases, where the differential cross-section is given by Eq. (35) with the normalized parameter $a = 1$ in Eq. (37). In each subfigure, from bottom to top (near $v_1 = 0$), the time t' for each line is 0, 2, 4, 6, 1, 8, 10, 12, and 80, respectively. (bottom row) The spatially-homogeneous relaxation of VDFs f^B for (d) Fermi, (e) classical, and (f) Bose gases. Note that in all the figures, the symbol ‘cross’ shows the equilibrium VDF given by Eq. (40). Due to symmetry only the region $v_1 > 0$ is shown.

297 When $N = 64$, from Fig. 3(a) we find that the mass is conserved to the machine accuracy.
 298 However, as N decreases, the mass is not strictly conserved, e.g. when $N = 24$. This is
 299 because the discretized frequency components do not cover the whole spectrum of VDF,
 300 such that some information is lost, and consequently the mass is not conserved; if higher
 301 accuracy is required when $N = 24$, the velocity domain should be reduced by decreasing the
 302 value of L such that the discretized frequency components will cover the whole spectrum
 303 of VDF, as from Eq. (21) we find that the range of the frequency is inversely proportional
 304 to L . From Fig. 3(b) we see that the energy (temperature) is not conserved, but the max-
 305 imum relative deviation from the initial value is about 10^{-5} when $N = 24$ and 10^{-6} when
 306 $N = 32$. Although the relative error generally increases with the order of moment, deviations
 307 of the sixth-order moment from reference solutions are still very small for the parameters
 308 considered.

309 4.2. The unequal-mass mixture

310 We now consider the case of unequal-mass mixture, where the molecular mass of the
 311 A-component m^A is 4 times of that of the B-component m^B . Due to the conservation of
 312 mass of each component and the total energy of the mixture, the initial condition (38) leads

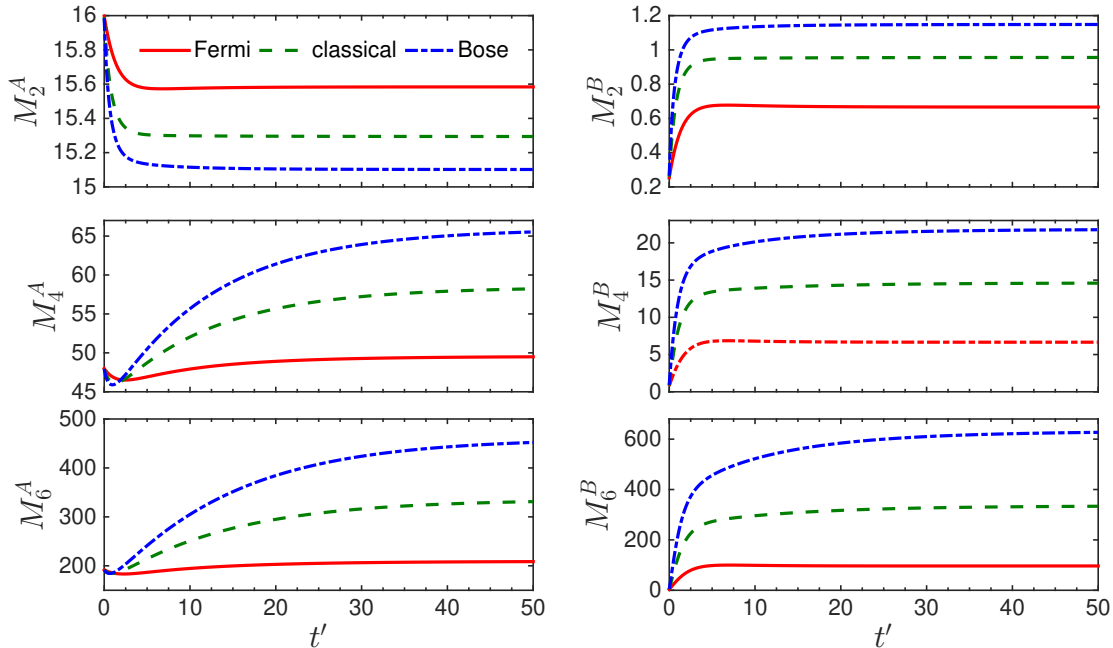


Figure 5: The relaxation of the second-, fourth-, and sixth-order moments of VDFs in the binary mixture with $m^A/m^B = 4$. Here the moments are defined as $M_l^i(t) = (m^i/m^A)^3 \int \int f^i(\mathbf{v}, t) |\mathbf{v}|^l d\mathbf{v}$, where $l = 2, 4$, and 6. Other parameters are the same as used in Fig. 4.

313 to the following equilibrium states:

$$f^i(t = \infty, \mathbf{v}) = \left\{ \frac{1}{Z^i} \exp\left(\frac{|\mathbf{v}|^2}{T}\right) - \theta_0 \right\}^{-1}, \quad (40)$$

314 where the fugacities Z^A and Z^B of each component and the temperature T of the mixture are
 315 $(Z^A, Z^B, T) = (7.9246, 0.7284, 1.1634)$, $(1.3320, 0.3330, 1.9118)$, and $(0.6461, 0.2287, 2.4516)$
 316 for Fermi, classical, and Bose gases, respectively. Note that for Bose gas, there is a compu-
 317 tational challenge, as under the fugacity limit $Z \rightarrow 1$, the viscosity decreases to zero and
 318 the equation becomes stiff so that the time step will be very small in explicit method; some
 319 implicit numerical methods may be used [37]. However, in this case $Z = 0.2287$ is much
 320 smaller than 1, so the simple explicit numerical method is used.

321 In the numerical simulation, the velocity space $[-L, L]^2$ with $L = 12$ is discretized by
 322 64×64 uniformly-distributed grid points: we choose $L = 12$ because the component B
 323 has a smaller molecular mass, so it requires larger velocity domain. For the component B,
 324 however, $N = 64$ and $L = 12$ is roughly equivalent to $N = 32$ and $L = 6$ in the equal-mass
 325 mixture in Sec. 4.1. We also choose $M = 5$ and $M_2 = 10$, as the accuracy is only improved
 326 slightly when the two values are doubled. These parameters should predict solutions with
 327 the same order of error as the case of $N = 32$ in the equal-mass case considered in Sec. 4.1,
 328 where the conservation of mass and total energy is preserved with the relative error less than
 329 10^{-8} and 10^{-6} , respectively.

330 The relaxation of the two initial VDFs (38) is depicted in Fig. 4, while the time evolution

331 of the second-, fourth-, and sixth-order moments are shown in Fig. 5. It is seen that near
 332 the region $v_1 = 0$, the VDF of component A increases monotonically with time, while that
 333 of the component B first increases rapidly, and then decreases as time t' goes by. This is
 334 due to the energy exchange between the two components: from the first row in Fig. 5 we
 335 see that the component B receives energy from the component A, so the width of VDF of
 336 component B has to increase while the value of VDF near $v_1 = 0$ has to decrease. When t'
 337 is large enough, the final equilibrium states have been achieved for both components, and
 338 the simulated VDFs agree well with the analytical solutions (40). Finally, when compared
 339 to the equal-mass mixture case without energy transfer between the two components, it is
 340 seen in Fig. 5 that the fourth- and sixth-order moments of the component A first decrease
 341 slightly, due to the energy output to the component B, and then increase with time, while
 342 those of the component B always increase until reach the corresponding equilibrium values.

343 It should be emphasized that the two numerical examples presented in this section only
 344 show the correctness of relaxation to final equilibrium states. However, whether the relax-
 345 ation process (i.e. the speed of relaxation) is accurately captured by the FSM or not is not
 346 clear, since we have no analytical solutions to compare with for quantum gases, although
 347 for the classical Boltzmann equation of Maxwell molecules (i.e. the intermolecular force
 348 is proportional to r^{-5} , where r is the intermolecular distance), the relaxation process has
 349 been verified by analytical BKW solutions [18, 24]. In the next section, we will assess the
 350 accuracy of FSM by comparing the numerical results of transport coefficients to analytical
 351 and numerical solutions presented in literature [38, 35, 36].

352 5. Transport coefficients

353 Compared to classical gases, transport coefficients of quantum gases are hard to measure
 354 experimentally. Therefore, an accurate and efficient method is urgently needed to solve the
 355 QBE. The transport coefficients such as shear viscosity, thermal conductivity, and diffusion
 356 can be calculated by means of the Chapman-Enskog expansion [7]. The basic idea of this
 357 expansion is to expand the VDF around the local equilibrium (8) in terms of a small pa-
 358 rameter related to the Knudsen number, which gives the Euler equations at the zeroth-order
 359 approximation. For the first-order approximation, i.e. a solution of Eq. (2) in the form of
 360 Eq. (11) is sought, the Navier-Stokes equations can be derived, where the small perturbation
 361 satisfies (in what follows we focus on two-component mixtures; detailed calculation can be
 362 found, e.g. in Ref. [38]):

$$\begin{aligned} \mathcal{L}^{ij}(h^i, h^j) = & \left\{ \frac{m^i}{k_B T} \sum_{ij} D_{ij}^i \left[v_{r,i} v_{r,i} - \frac{\delta_{ij}}{d_v} |\mathbf{v}_r|^2 \right] + \mathbf{v}_r \cdot \mathbf{d}^i \right. \\ & \left. + \frac{\mathbf{v}_r \cdot \nabla_{\mathbf{x}} T}{T} \left[\frac{m^i |\mathbf{v}_r|^2}{2k_B T} - \frac{d_v + 2}{2} \frac{G_{(d_v+2)/2}(Z^i)}{G_{d_v/2}(Z^i)} \right] \right\} f_{eq}^i (1 + \theta_0 f_{eq}^i), \end{aligned} \quad (41)$$

363 where $D_{ij} = (\partial V_j / \partial x_i + \partial V_i / \partial x_j) / 2$ is the rate-of-strain tensor. Note that the first, second,
 364 and third terms on the right-hand side of Eq. (41) are related to the shear viscosity, diffusion,
 365 and thermal conductivity, respectively. Since the definition of the coefficient of mass diffusion

366 refers to a state of gas in which no external forces act on the molecules, and the gas pressure
 367 and temperature are uniform [7], the complicated expression for \mathbf{d}^i is simplified to $\mathbf{d}^i =$
 368 $\frac{\nabla_{\mathbf{x}} Z^i}{Z^i} = \frac{\nabla_{\mathbf{x}} \mu^i}{k_B T}$ [38].

369 The constitutive relations at the first-order Chapman-Enskog expansion are given by

$$P = \sum_i \delta_{ij} P_{ij}^i - 2\eta \left[D_{ij} - \frac{\text{Tr}(D_{ij})}{d_v} \delta_{ij} \right], \quad \mathbf{Q} = -\kappa \nabla T, \quad \mathbf{J}_M = -D \nabla M, \quad (42)$$

370 where P is the total pressure of the mixture, and \mathbf{J}_M is the mass current induced by the
 371 population difference $M = n^i - n^j$.

372 The shear viscosity η , thermal conductivity κ , and mass diffusion coefficient D can be
 373 found in the following three steps. First, we obtain the perturbation functions h by solving
 374 the following equations (the detailed methods will be presented in following subsections):

$$\mathcal{L}^{ij}(h^i, h^j) = f_{eq}^i (1 + \theta_0 f_{eq}^i) \frac{m^i}{k_B T} D_{ij}^i \left[v_{r,i} v_{r,i} - \frac{\delta_{ij}}{d_v} |\mathbf{v}_r|^2 \right], \quad (43)$$

$$\mathcal{L}^{ij}(h^i, h^j) = f_{eq}^i (1 + \theta_0 f_{eq}^i) \frac{\mathbf{v}_r \cdot \nabla T}{T} \left[\frac{m^i |\mathbf{v}_r|^2}{2k_B T} - \frac{d_v + 2}{2} \frac{G_{(d_v+2)/2}(Z^i)}{G_{d_v/2}(Z^i)} \right], \quad (44)$$

$$\mathcal{L}^{ij}(h^i, h^j) = f_{eq}^i (1 + \theta_0 f_{eq}^i) \frac{\mathbf{v}_r \cdot \nabla_{\mathbf{x}} \mu^i}{k_B T}. \quad (45)$$

375 For simplicity, in the following calculations, we define terms on the right-hand sides of
 376 Eqs. (43)-(45) as the source \mathcal{S}^i . Second, with h , we can calculate the total pressure P , heat
 377 flux \mathbf{Q} , and mass current \mathbf{J}_M according to Eqs. (11) and Eq. (1). Finally, from Eq. (42) we
 378 can obtain the transport coefficients.

379 5.1. Variational principles

380 The complicated mathematical structure of the linearized Boltzmann collision operator
 381 \mathcal{L}^{ij} makes the exact solution for the perturbation h in Eqs. (43)-(45) extremely difficult
 382 to find. Therefore, variational principles are used to find the upper and lower bounds of
 383 transport coefficients [39]. A simple way is to use the following ansatz:

$$h^i = C^i \mathcal{S}^i, \quad i = A, B, \quad (46)$$

384 where C^i are constants, whose values can be obtained by solving the following two linear
 385 equations of C^A and C^B :

$$\int \mathcal{L}^{ij}(C^i \mathcal{S}^i, C^j \mathcal{S}^j) \frac{\mathcal{S}^i}{f_{eq}^i (1 + \theta_0 f_{eq}^i)} d\mathbf{v} = \int \frac{(\mathcal{S}^i)^2}{f_{eq}^i (1 + \theta_0 f_{eq}^i)} d\mathbf{v}, \quad i = A, B. \quad (47)$$

386 Expressions for the two constants C^A and C^B can be simplified analytically, and then
 387 solved by numerical quadrature (for the classical Boltzmann equation with some special
 388 forms of differential cross-section, analytical solution may be derived), see Eq. (49) below.
 389 Also, C^A and C^B can be computed by the FSM developed in this paper.

390 The variational principle (46) predicts the lower bound of transport coefficients. For the
 391 classical Boltzmann equation, this variational principle gives accurate transport coefficients
 392 for Maxwell molecules, while for hard-sphere molecules it underpredicts the transport coef-
 393 ficients by only about 2 % [7]. Whether this conclusion holds for quantum gases or not is
 394 not clear; this will be assessed in the following numerical examples.

395 5.2. Direct numerical simulation

396 A direct numerical solution of the linear equations in Eqs. (43)-(45) is necessary to find
 397 accurate transport coefficients. To this end, we first define the following two constants as
 398 the maximum values of the equilibrium collision frequencies in Eq. (13), for classical gases:
 399 $\mu^\iota = \sum_j \mu_c^{ij}(\mathbf{v} = 0)$ with $\iota = A, B$. Then, the linear perturbation can be solved through the
 400 following iterative scheme [17]:

$$h^{i,\iota+1} = \frac{-\mathcal{S}^\iota + \mathcal{L}^{ij}(h^{i,\iota}, h^{j,\iota}) + \mu^\iota h^i}{\mu^\iota}, \quad \iota = A, B, \quad (48)$$

401 where the superscripts ι and $\iota + 1$ are the iteration steps.

402 The reason to use μ^ι in the denominator of Eq. (48) instead of the equilibrium collision
 403 frequency μ_c^{ij} , as normally used in the iterative scheme [17], is that the collision frequency
 404 approximated by the FSM approaches zero at large relative collision velocity \mathbf{u} for the special
 405 differential cross-section (35). Therefore, the iteration will diverge when μ_c^{ij} is used in the
 406 denominator. Numerical simulations below have proven that the iterative scheme (48) is
 407 unconditionally stable, while using μ_c^{ij} in the denominator results in non-converged solution
 408 when the quantum gas is highly degenerated, that is, when the fugacity Z approaches infinity
 409 and one for Fermi and Bose gases, respectively.

410 In the following numerical simulations, the iteration is terminated until the relative error
 411 in the transport coefficient between two consecutive steps is less than 10^{-5} . Starting from
 412 the zero perturbation $h^{i,\iota=0} = 0$, only several dozen iterations are needed to reach this
 413 convergence criterion.

414 5.3. Results: three-dimensional case

415 We consider the two-component population balanced Fermi gases, with $m^A = m^B = m$.
 416 In most experiments, the two components move together and only one VDF is enough to
 417 describe the system state. Due to Pauli's exclusion principle, the s -wave scattering happens
 418 between molecules with different spins. As a consequence, only the cross-collision operators
 419 are considered. For simplicity, the hard-sphere molecular model is used, where the differential
 420 cross-section is $d\sigma^{ij}/d\Omega = a_s^2$.

421 Applying the Chapman-Enskog expansion to the QBE, one obtains the shear viscosity
 422 and thermal conductivity as [38]

$$\eta = \frac{5m}{32a_s^2 I_B} \sqrt{\frac{k_B T}{m}} G_{5/2}^2(Z), \quad \kappa = \frac{75k_B}{256a_s^2 I_A} \sqrt{\frac{k_B T}{m}} \left[\frac{7}{2} G_{7/2}(Z) - \frac{5}{2} \frac{G_{5/2}^2(Z)}{G_{3/2}(Z)} \right]^2, \quad (49)$$

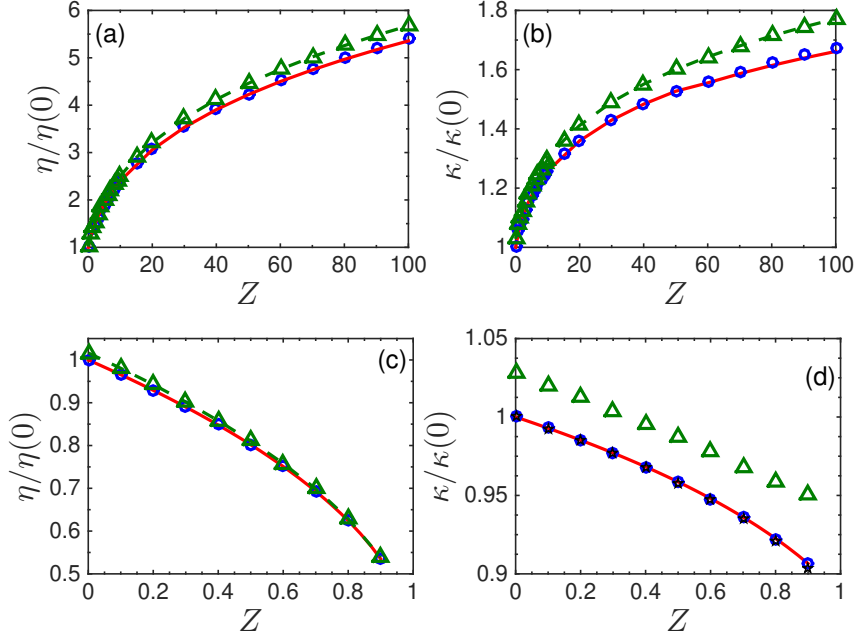


Figure 6: The shear viscosity η and thermal conductivity κ of Fermi (top row) and Bose (bottom row) gases, as functions of the fugacity Z , where η_0 and κ_0 are respectively the shear viscosity and thermal conductivity at the classical limit $Z = 0$, which are obtained from the analytical solution (49) that is derived from the variational principle [40, 38]. Solid lines: analytical solutions (49). Circles: numerical solutions using the variational principle, i.e. by solving Eq. (47) numerically via the FSM. Triangles: numerical results obtained by solving Eq. (48) via the FSM.

423 where

$$\begin{aligned}
 I_A &= \int_0^\infty d\xi_0 \xi_0^4 \int_0^\infty d\xi' \xi'^7 \int_0^1 dy' \int_0^1 dy'' F \cdot (y'^2 + y''^2 - 2y'^2 y''^2), \\
 I_B &= \int_0^\infty d\xi_0 \xi_0^2 \int_0^\infty d\xi' \xi'^7 \int_0^1 dy' \int_0^1 dy'' F \cdot (1 + y'^2 + y''^2 - 3y'^2 y''^2), \\
 F &= \frac{Z^2 \exp(-\xi_0^2 - \xi'^2)}{[1 - \theta_0 Z \exp(-\xi_1^2)][1 - \theta_0 Z \exp(-\xi_2^2)][1 - \theta_0 Z \exp(-\xi_3^2)][1 - \theta_0 Z \exp(-\xi_4^2)]},
 \end{aligned}$$

424 $\xi_1^2 = (\xi_0^2 + 2\xi_0 \xi' y' + \xi'^2)/2$, $\xi_2^2 = (\xi_0^2 - 2\xi_0 \xi' y' + \xi'^2)/2$, $\xi_3^2 = (\xi_0^2 + 2\xi_0 \xi' y'' + \xi'^2)/2$, and
 425 $\xi_4^2 = (\xi_0^2 - 2\xi_0 \xi' y'' + \xi'^2)/2$.

426 For the one-component Bose gas, the differential cross-section is $d\sigma^{vj}/d\Omega = 2a_s^2$ [40], so
 427 the shear viscosity and thermal conductivity will be four times smaller than that of the
 428 population balanced Fermi gas, because both the self- and cross-collision operators have to
 429 be considered.

430 Figure 6 shows the shear viscosity and thermal conductivity of quantum Fermi and
 431 Bose gases as functions of the fugacity. It is seen that the shear viscosity and thermal
 432 conductivity of the Fermi (Bose) gas increase (decrease) with the fugacity Z . The FSM
 433 solutions of variational equation (47) agree well with the analytical solutions (49) obtained

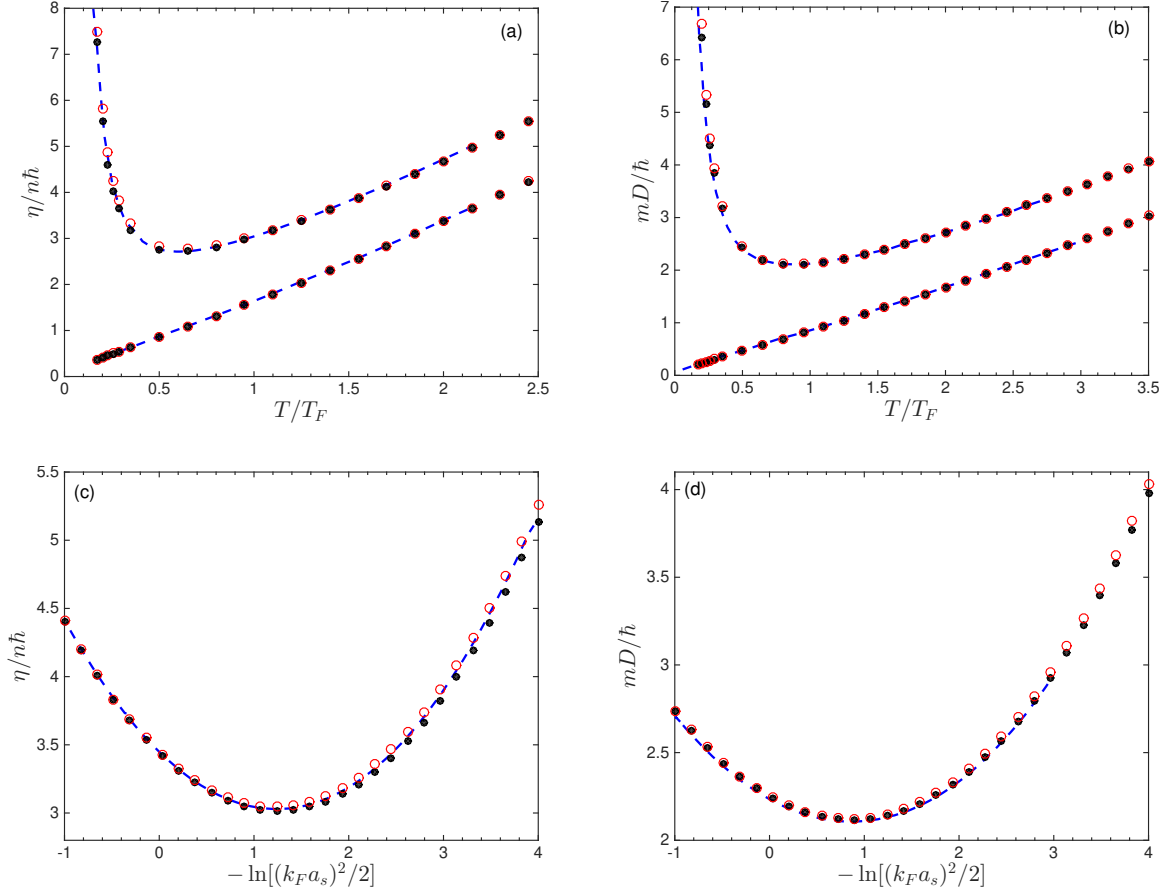


Figure 7: The normalized shear viscosity (a, c) and mass diffusion coefficient (b, d) of 2D Fermi gas as functions of the (a, b) normalized temperature T/T_F at $(k_F a_s)^2 = 2 \exp(-1)$ and (c, d) s-wave scattering length a_s at $T/T_F = 1$. Dashed lines represent results from the variation principle adopted from Ref. [35]. Solid circles: FSM solutions of the variational principle (47). Open circles: the FSM solutions obtained by the iterative scheme (48). Nearly-straight lines in (a) and (b) are the corresponding results for classical gases. Note that $T_F = (\hbar k_F)^2 / 2mk_B$ is the Fermi temperature, and $k_F = \sqrt{2\pi n}$ is the Fermi wave vector, with n being the total number density of both spin components.

434 by the same variational principle, which proves that our FSM has high accuracy.

435 With the accuracy of the FSM verified by analytical solutions, we assess the accuracy
 436 of the variational principle that only gives the lower bounds of transport coefficients, by
 437 solving the linearized equation using the iterative method (48). Results are shown in Fig. 6
 438 as triangles. For Fermi gas, at Z increases from 0 to 100, the relative error between the
 439 accurate shear viscosity (thermal conductivity) and those from the variational principle
 440 increases from 1.6% (2.8%) to 5.2% (6%). For Bose gas, this relative error in thermal
 441 conductivity increases from about 2.8% when $Z = 0$ to 5.2% when $Z = 0.9$, while that in
 442 shear viscosity decreases from 1.6% when $Z = 0$ to 0.2% when $Z = 0.9$.

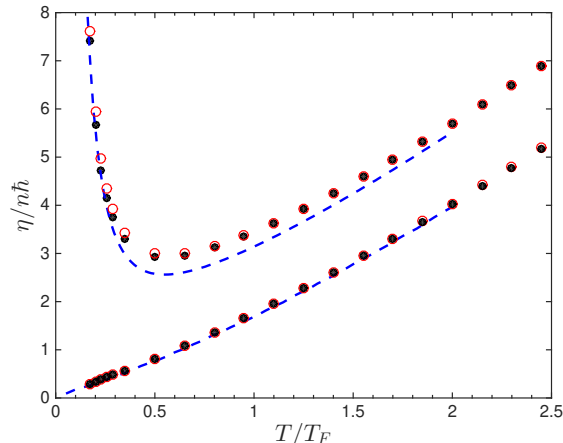


Figure 8: The normalized shear viscosity of 2D Fermi gas as a function of the temperature, where the interaction strength between fermions with equal mass but opposite spins is $(k_F a_s)^2 = 2$. Dashed lines represent results from the variation principle adopted from Ref. [36]. Solid circles: the FSM solutions of the variational principle (47). Open circles: the FSM solutions of the iterative scheme (48).

443 5.3.1. Shear viscosity of the mass-balanced mixture

444 We first consider the equal-mass mixture, i.e. $m^A = m^B = m$. Numerical results for
 445 the shear viscosity and spin diffusion coefficients are shown in Fig. 7, for a wide range of
 446 temperature and s-wave scattering length. It is clear that the variational solutions solved by
 447 the FSM agree well with the numerical solutions of Brunn [35] for both classical and Fermi
 448 gases, while the accurate shear viscosity and mass diffusion coefficient obtained from the
 449 iterative scheme (48) have very limited difference to the variational solutions (i.e. less than
 450 1%) when $T/T_F < 1$. However, at very small values of T/T_F , accurate transport coefficients
 451 are larger than the variational ones by about 5% for Fermi gas. This observation is consistent
 452 with the 3D Fermi gas case investigated in Sec. 5.3.

453 We continue to compare our FSM solutions to the numerical solutions provided by
 454 Schäfer [36] in Fig. 8. The agreement is acceptable in general, especially for the case of
 455 classical gases. For Fermi gases, the shear viscosity obtained from the FSM agrees well
 456 with the variational solutions [36] in the low and high temperature limits. However, in the
 457 intermediate regime (near $T/T_F = 0.5$) where the shear viscosity is minimum, both of our
 458 FSM solutions, obtained from the variational principle (47) and the iterative scheme (48),
 459 are higher than the variational results of Schäfer [36] by about 15%.

460 5.3.2. Shear viscosity of mass-imbalanced mixtures

461 We further calculate the shear viscosity of the equal-mole mixture of 2D Fermi gas, where
 462 the A-component has a larger molecular mass than the B-component. In Fig. 9 the shear
 463 viscosity when $m^A/m^B = 1, 2, 4,$ and $40/6$ is plotted. It is observed in Fig. 9(a) that, when
 464 the s-wave scattering length is fixed, that is, when the ratio of the two-body binding energy
 465 $E_b = 1/2m_r a_s^2$ to the Fermi energy of A-component is equal to $\exp(1)$, the shear viscosity
 466 first decreases when the temperature increases, and then increases with the temperature,
 467 for all the molecular mass ratios considered. However, the reduced temperature T/T_F at

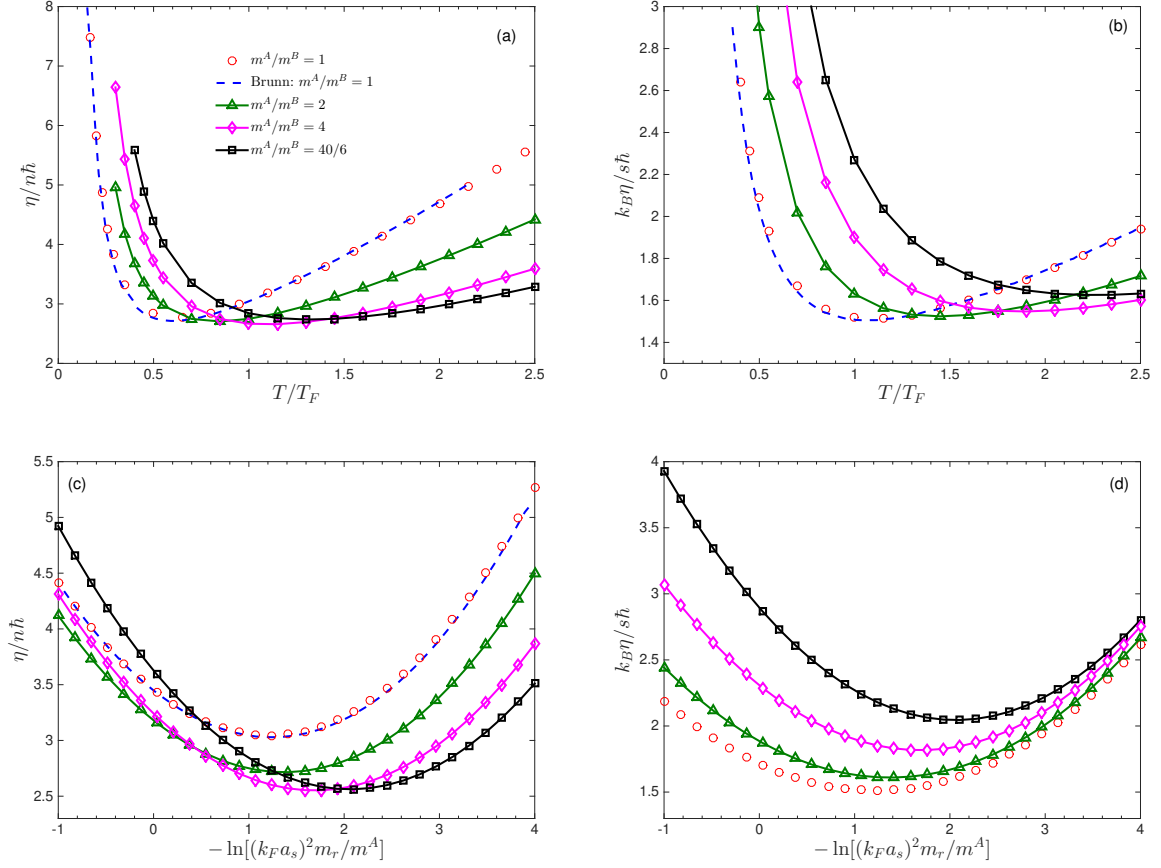


Figure 9: The shear viscosity of equal-mole mixture of 2D quantum Fermi gas, where the molecular mass of each components are different. The shear viscosity (a) and viscosity-entropy ratio (b) of 2D Fermi gas as a function of the normalized temperature T/T_F at $(k_F a_s m_r / m^A)^2 = \exp(-1)$. The shear viscosity (c) and viscosity-entropy density ratio (d) of 2D Fermi gas as functions of the s-wave scattering length $(k_F a_s m_r / m^A)^2$ when $T/T_F = 1$. Symbols: the FSM solutions of the iterative scheme (48). Note that $T_F = (\hbar k_F)^2 / 2m^A k_B$ is the Fermi temperature of A-component, and $k_F = \sqrt{2\pi n}$ is the Fermi wave vector, with n being the total number density of both spin components.

468 which the minimum shear viscosity is reached increases with the mass ratio. The same trend
 469 applies also to the viscosity-entropy density ratio in Fig. 9(b). Interestingly, in Fig. 9(a)
 470 we see that the minimum shear viscosity almost remains unchanged when the molecular
 471 mass ratio varies; this is in sharp contrast to the variational results [35], which states that
 472 the shear viscosity is proportional to the reduced mass, i.e. decreases when the mass ratio
 473 increases. This discrepancy may be caused by the fact that the variational ansatz used in
 474 Eq. (4) of Ref. [35] is different to ours in Eq. (46) when the molecular mass ratio is not one.

475 Figure 9(c) shows the variation of the shear viscosity against the interaction strength,
 476 when the temperature of the mixture is equal to the Fermi temperature of A-component.
 477 When the molecular mass ratio is fixed, there is a minimum value of shear viscosity; and
 478 it seems that this minimum viscosity decreases when the mass ratio increases, but quickly
 479 saturated at $m^A/m^B = 40/6$. In addition, at small enough interaction strength, i.e. in

480 the right part of Fig. 9(c), the shear viscosity decreases when the molecular mass ratio
 481 increases, while at large interaction strength, there is no monotonous relation between the
 482 shear viscosity and mass ratio.

483 Figure 9(b) and (d) depict the ratio between the shear viscosity and entropy density. It
 484 is clear that the minimum viscosity-entropy ratio does not change much when the molecular
 485 mass ratio varies. Although Brunn [35] claimed that the universal bound of the viscosity-
 486 entropy density ratio obtained from string theory methods [41]

$$\frac{k_B \eta}{s \hbar} > \frac{1}{4\pi} \quad (50)$$

487 may be violated at large molecular mass ratios, our numerical calculations suggested this is
 488 not the case, at least for the QBE with the differential cross-section (35).

489 6. Conclusions

490 We have developed a FSM to solve the quantum Boltzmann equation for gas mixtures
 491 with a computational cost of $O(M^{d_v-1} M_2 N^{d_v} \log N)$, which is the same as that for the classi-
 492 cal Boltzmann equation when the general form of intermolecular potential is considered [17].
 493 The spatially-homogeneous relaxation problem has been used to determine factors that af-
 494 fect the accuracy of FSM. It has been shown that, the solid angle (or polar angle in the
 495 two-dimensional problem) can be discretized uniformly by $M^2 = 5 \times 5$ (or $M = 5$) points,
 496 while the number of abscissas in the Gauss-Legendre quadrature used in Eq. (24) can be as
 497 small as $M_2 = 10$, when $N = 32$ velocity points are used to discretize the velocity distribu-
 498 tion function in each direction. The FSM handles the collision in the frequency space, and
 499 conserves the mass exactly, while the momentum and energy are conserved with spectral
 500 accuracy.

501 Based on the variational principle that predicts the lower bounds of transport coefficients,
 502 the shear viscosity and thermal conductivity have been calculated by the FSM for both Fermi
 503 and Bose gases. Comparisons with the analytical solutions demonstrated the accuracy of the
 504 proposed FSM. Accurate transport coefficients are also obtained by solving the linearized
 505 Boltzmann collision operator via the iterative scheme (48). As expected, these transport
 506 coefficients are larger than those from the variational principle. Generally speaking, the
 507 relative error between the accurate and variational transport coefficients increases with the
 508 fugacity. The shear viscosity of a two-dimensional equal-mole mixture of Fermi gases has also
 509 been investigated for components with different molecular masses. Our numerical solutions
 510 suggested that the universal bound of the viscosity-entropy density ratio (50) predicted by
 511 the string theory is satisfied.

512 Finally, we pointed that the established accurate FSM to solving the quantum Boltzmann
 513 collision operator is ready to be used to calculate the transport coefficients of noble gases
 514 based on *ab initio* potentials [42, 43]. Also, the FSM can be used to assess the accuracy of
 515 quantum kinetic models [44, 45, 46]. Furthermore, the FSM can be incorporated into other
 516 multi-scale methods [47, 48, 37] that solve the Boltzmann equation accurately and efficiently
 517 from the hydrodynamic to free-molecular flow regimes, which is encountered in experiments

518 where the quantum gas is trapped so that its density is maximum at the trap center (i.e.
519 hydrodynamic regime) and vanishes near the trap edge (i.e. free molecular flow regime). In
520 the future we will investigate the interesting spatially-inhomogeneous oscillations [12, 13, 14]
521 and spin diffusion [30, 31, 32] in quantum gases.

522 Acknowledgments

523 This work is financially supported by the UK's Engineering and Physical Sciences Re-
524 search Council (EPSRC) under grant EP/R041938/1.

525 References

- 526 [1] F. Dalfovo, S. Giorgini, L. P. Pitaevskii, S. Stringari, Theory of Bose-Einstein condensation in trapped
527 gases, *Rev. Mod. Phys.* 71 (1999) 463.
- 528 [2] M. H. Anderson, J. R. Ensher, M. R. Matthews, C. E. Wieman, E. A. Cornell, Observation of Bose-
529 Einstein condensation in a dilute atomic vapor, *Science* 269 (1995) 198–201.
- 530 [3] M. Greiner, C. A. Regal, D. S. Jin, Emergence of a molecular Bose–Einstein condensate from a Fermi
531 gas, *Nature* 426 (2003) 537–540.
- 532 [4] E. A. Uehling, G. E. Uhlenbeck, Transport phenomena in Einstein-Bose and Fermi-Dirac gases. I, *Phys.*
533 *Rev.* 43 (1933) 0552–0561.
- 534 [5] B. Jackson, E. Zaremba, Finite-temperature simulations of the scissors mode in Bose-Einstein condensed
535 gases, *Phys. Rev. Lett.* 87 (2001) 100404.
- 536 [6] B. Jackson, E. Zaremba, Modeling Bose-Einstein condensed gases at finite temperature with N-body
537 simulations, *Phys. Rev. A* 66 (2002) 033606.
- 538 [7] S. Chapman, T. Cowling, *The Mathematical Theory of Non-uniform Gases*, Cambridge University
539 Press, 1970.
- 540 [8] A. L. Garcia, W. Wagner, Direct simulation Monte Carlo method for the Uehling-Uhlenbeck-Boltzmann
541 equation, *Phys. Rev. E* 68 (2003) 056703.
- 542 [9] G. A. Bird, *Molecular Gas Dynamics and the Direct Simulation of Gas Flows*, Oxford Science Publi-
543 cations, Oxford University Press Inc, New York, 1994.
- 544 [10] P. Borowik, J. Thobel, L. Adamowicz, Modified Monte Carlo method for study of electron transport
545 in degenerate electron gas in the presence of electron-electron interactions, application to graphene, *J.*
546 *Comput. Phys.* 341 (2017) 397–405.
- 547 [11] R. Yano, Fast and accurate calculation of dilute quantum gas using Uehling-Uhlenbeck model equation,
548 *J. Comput. Phys.* 330 (2017) 1010–1021.
- 549 [12] E. Vogt, M. Feld, B. Fröhlich, D. Pertot, M. Koschorreck, M. Köhl, Scale invariance and viscosity of a
550 two-dimensional Fermi gas, *Phys. Rev. Lett.* 108 (2012) 070404.
- 551 [13] L. Wu, Y. H. Zhang, Numerical investigation of the radial quadrupole and scissors modes in trapped
552 gases, *Europhys. Lett.* 97 (2012) 16003.
- 553 [14] L. Wu, Y. H. Zhang, Applicability of the Boltzmann equation for a two-dimensional Fermi gas, *Phys.*
554 *Rev. A* 85 (2012) 045601.
- 555 [15] C. Mouhot, L. Pareschi, Fast algorithms for computing the Boltzmann collision operator, *Math. Comput.*
556 75 (2006) 1833–1852.
- 557 [16] F. Filbet, C. Mouhot, L. Pareschi, Solving the Boltzmann equation in $N \log N$, *SIAM J. Sci. Comput.*
558 28 (2006) 1029–1053.
- 559 [17] L. Wu, H. H. Liu, Y. H. Zhang, J. M. Reese, Influence of intermolecular potentials on rarefied gas flows:
560 Fast spectral solutions of the Boltzmann equation, *Phys. Fluids* 27 (2015) 082002.
- 561 [18] L. Wu, C. White, T. J. Scanlon, J. M. Reese, Y. H. Zhang, Deterministic numerical solutions of the
562 Boltzmann equation using the fast spectral method, *J. Comput. Phys.* 250 (2013) 27–52.

- 563 [19] L. Wu, J. M. Reese, Y. H. Zhang, Solving the Boltzmann equation by the fast spectral method:
564 application to microflows, *J. Fluid Mech.* 746 (2014) 53–84.
- 565 [20] L. Wu, J. Zhang, H. H. Liu, Y. H. Zhang, J. M. Reese, A fast iterative scheme for the linearized
566 Boltzmann equation, *J. Comput. Phys.* 338 (2017) 431–451.
- 567 [21] L. Wu, J. M. Reese, Y. H. Zhang, Oscillatory rarefied gas flow inside rectangular cavities, *J. Fluid
568 Mech.* 748 (2014) 350–367.
- 569 [22] L. Wu, Sound propagation through a rarefied gas in rectangular channels, *Phys. Rev. E* 94 (2016)
570 053110.
- 571 [23] L. Wu, C. White, T. J. Scanlon, J. M. Reese, Y. H. Zhang, A kinetic model of the Boltzmann equation
572 for nonvibrating polyatomic gases, *J. Fluid Mech.* 763 (2015) 24–50.
- 573 [24] L. Wu, J. Zhang, J. M. Reese, Y. H. Zhang, A fast spectral method for the Boltzmann equation for
574 monatomic gas mixtures, *J. Comput. Phys.* 298 (2015) 602–621.
- 575 [25] M. T. Ho, L. Wu, I. A. Graur, Y. H. Zhang, J. M. Reese, Comparative study of the Boltzmann and
576 McCormack equations for Couette and Fourier flows of binary gaseous mixtures, *Int. J. Heat Mass
577 Flow* 96 (2016) 29–41.
- 578 [26] L. Wu, Y. Zhang, J. M. Reese, Fast spectral solution of the generalized Enskog equation for dense
579 gases, *J. Comput. Phys.* 303 (2015) 66–79.
- 580 [27] L. Wu, H. H. Liu, J. M. Reese, Y. H. Zhang, Non-equilibrium dynamics of dense gas under tight
581 confinement, *J. Fluid Mech.* 794 (2016) 252–266.
- 582 [28] F. Filbet, J. Hu, S. Jin, A numerical scheme for the quantum Boltzmann equation with stiff collision
583 terms, *Math. Model. Num. Anal.* 46 (2012) 443–463.
- 584 [29] J. Hu, L. Ying, A fast spectral algorithm for the quantum Boltzmann collision operator, *Commun.
585 Math. Sci.* 10 (2012) 989–999.
- 586 [30] A. Sommer, M. Ku, G. Roati, M. W. Zwierlein, Universal spin transport in a strongly interacting Fermi
587 gas, *Nature* 472 (2011) 201–204.
- 588 [31] A. Sommer, M. Ku, M. W. Zwierlein, Spin transport in polaronic and superfluid Fermi gases, *New J.
589 Phys.* 13 (2011) 055009.
- 590 [32] M. Koschorreck, D. Pertot, E. Vogt, M. Köhl, Universal spin dynamics in two-dimensional Fermi gas,
591 *Nat. Phys.* 9 (2013) 405–409.
- 592 [33] L. Wu, H. Struchtrup, Assessment and development of the gas kinetic boundary condition for the
593 Boltzmann equation, *J. Fluid Mech.* 823 (2017) 511–537.
- 594 [34] L. Pareschi, G. Russo, Numerical solution of the Boltzmann equation I: Spectrally accurate approxi-
595 mation of the collision operator, *SIAM J. Numer. Anal.* 37 (2000) 1217–1245.
- 596 [35] G. M. Bruun, Shear viscosity and spin-diffusion coefficient of a two-dimensional Fermi gas, *Phys. Rev.
597 A* 85 (2012) 013636.
- 598 [36] T. Schäfer, Shear viscosity and damping of collective modes in a two-dimensional Fermi gas, *Phys. Rev.
599 A* 85 (2012) 033623.
- 600 [37] F. Filbet, J. Hu, J. Shi, A numerical scheme for the quantum Boltzmann equation efficient in the fluid
601 regime, arxiv:1009.3352v1.
- 602 [38] S. Watabe, A. Osawa, T. Nikuni, Zero and first sound in normal Fermi systems, *J. Low Temp. Phys.*
603 158 (2010) 773–805.
- 604 [39] H. Smith, H. H. Jensen, *Transport Phenomena*, Oxford University Press, 1989.
- 605 [40] T. Nikuni, A. Griffin, Hydrodynamic damping in trapped Bose gases, *J. Low Temp. Phys.* 111 (1998)
606 793–814.
- 607 [41] P. K. Kovtun, D. T. Son, A. O. Starinets, Viscosity in strongly interacting quantum field theories from
608 black hole physics, *Phys. Rev. Lett.* 94 (2005) 111601.
- 609 [42] B. Song, X. Wang, J. Wu, Z. Liu, Prediction of transport properties of pure noble gases and some of
610 their binary mixtures by ab initio calculations, *Fluid Phase Equilibria* 290 (2010) 55–62.
- 611 [43] F. Sharipov, V. J. Benites, Transport coefficients of helium-neon mixtures at low density computed
612 from ab initio potentials, *J. Chem. Phys.* 147 (2017) 224302.
- 613 [44] L. Wu, J. P. Meng, Y. H. Zhang, Kinetic modelling of the quantum gases in the normal phase, *Proc.*

- 614 R. Soc. A 468 (2012) 1799–1823.
- 615 [45] J. Y. Yang, C. Y. Yan, M. Diaz, J. C. Huang, Z. H. Li, H. X. Zhang, Numerical solutions of ideal
616 quantum gas dynamical flows governed by semiclassical ellipsoidal-statistical distribution, Proc. R.
617 Soc. A 470 (2013) 20130413.
- 618 [46] M. A. Diaz, J. Y. Yang, An efficient direct solver for rarefied gas flows with arbitrary statistics, J.
619 Comput. Phys. 305 (2016) 127–149.
- 620 [47] C. Liu, K. Xu, Q. H. Sun, Q. D. Cai, A unified gas-kinetic scheme for continuum and rarefied flows IV:
621 Full Boltzmann and model equations, J. Comput. Phys. 314 (2016) 305–340.
- 622 [48] T. B. Xiao, Q. D. Cai, K. Xu, A well-balanced unified gas-kinetic scheme for multiscale flow transport
623 under gravitational field, J. Comput. Phys. 332 (2017) 475–491.